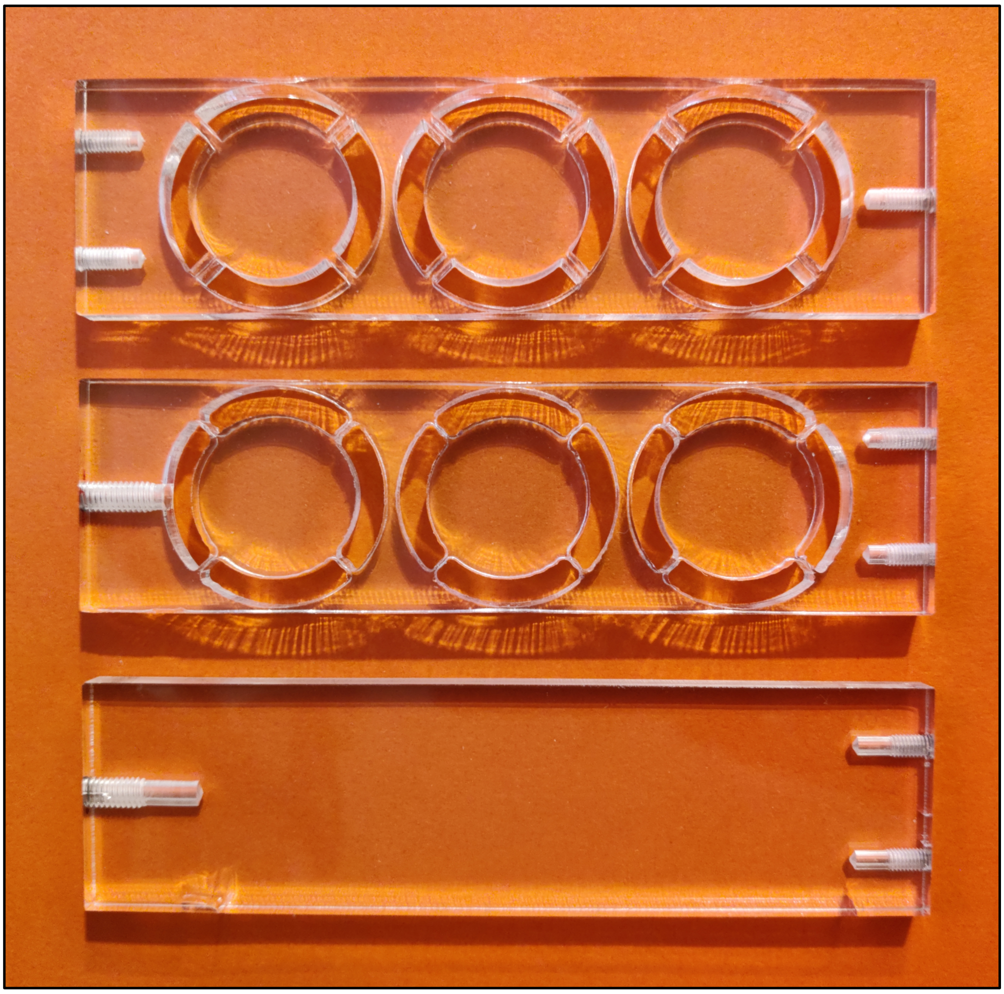

Development of Acoustic Metamaterial Vibrational Shields for Application at Cryogenic Temperatures

Master's thesis in Engineering Physics

EINAR CARLSSON

DEPARTMENT OF MICROTECHNOLOGY AND NANOSCIENCE
CHALMERS UNIVERSITY OF TECHNOLOGY
Gothenburg, Sweden 2026
www.chalmers.se

Master's thesis 2026

Development of Acoustic Metamaterial Vibration Shields for Application at Cryogenic Temperatures

EINAR CARLSSON

Department of Microtechnology and Nanoscience
Division of Quantum Technology
Quantum Sensing and Foundations Lab
Chalmers University of Technology
Gothenburg, Sweden 2026

Development of Acoustic Metamaterial Vibrational Shields for Application at Cryogenic Temperatures

EINAR CARLSSON

Supervisors: Thomas Penny and Fabian Resare, Department of Microtechnology and Nanoscience (MC2)
Examiner: Witlef Wieczorek, Department of Microtechnology and Nanoscience (MC2)

Master's Thesis 2026
Department of Microtechnology and Nanoscience
Division of Quantum Technology
Quantum Sensing and Foundations Lab
Chalmers University of Technology
SE-412 96 Gothenburg
Telephone +46 31 772 1000

Cover: Fabricated acoustic metamaterials (top and centre) for use in experimental characterization of vibration isolation along with bulk sample reference (bottom).

Typeset in LaTeX
Printed by Chalmers Reproservice
Gothenburg, Sweden 2026

Development of Acoustic Metamaterial Vibrational Shields for Application at Cryogenic Temperatures

EINAR CARLSSON
Department of Microtechnology and Nanoscience
Chalmers University of Technology

Abstract

Phononic crystals and acoustic metamaterials are prominent areas of research in the fields of acoustics and solid mechanics. These materials allow for the manipulation and suppression of elastic waves, for example sound waves in air or vibrational waves in solids. In particular, the mitigation of vibrational waves is of interest, with even small vibrations potentially causing noise in some low temperature experiments. In this thesis phononic crystals are presented as a method of vibration isolation at cryogenic temperatures.

The design and development of the acoustic metamaterials was guided by numerical simulations performed using the finite element method (FEM), where band structures were optimized and designed for a suitable geometry and material composition. Two of the simulated designs were fabricated with acrylic plastic and characterized using optical interferometry. By comparing the motion of the metamaterials with a reference bulk material the attenuation caused by it could be determined, resulting in an upper bound of 15 to 20 dB in attenuation across a frequency interval of roughly 7.0–11.0 kHz. Simulated metamaterials show encouraging results with band gap generation at frequencies below 4 kHz through careful considerations of the utilised materials. Further work is required to realise the experimental implementation, with reducing the noise floor of the interferometry measurements of particular importance, along with producing and testing more samples.

Keywords: phononic crystal, acoustic metamaterial, elasticity, vibration isolation, optical interferometry.

Acknowledgements

Firstly, I'd like to thank Prof. Witlef Wieczorek for giving me this opportunity to work in this fantastic group for these past six months as well as provide me with insights on the fascinating research you have all been doing. I am also grateful for the fantastic support of my two supervisors: Tom and Fabian, who have guided me along every step during this thesis, supporting and teaching me so much about your own work and how you choose to tackle problems that arise. Finally, I'd like to thank the rest of the team: Rishab, Albert, Joram, Alireza, Alexander, Anastasiia, Aditi, Achintya, and Paul. You have all welcomed me into the group and made this a very enjoyable six months. Thanks also to Lars Jönsson for helping with the fabrication of essential parts for this project.

Einar Carlsson, Gothenburg, July 2026

Contents

List of Figures

List of Tables

1

Introduction

Vibration isolation is a vital component in many fields of science and engineering with vibrations impacting measurements and other operations on all levels, from earthquakes to imperceptible vibrations in precision measurement setups. Phononic crystals, and acoustic metamaterials, are materials which aim to solve some of these issues by manipulating and controlling these vibrations via highly engineered patterns, geometries, and materials [1, 2]. Research on this topic is widespread [3–5], with breakthroughs in so-called acoustic metamaterials [6], i.e., materials which manipulate waves on a scale smaller than the acoustic wavelength in the material. These metamaterials are of significant importance, as they allow for lower frequencies to be manipulated, something which is usually limited by the size of phononic crystals.

There are many different fields and applications that acoustic metamaterials could be beneficial, with, for example, acoustic superlenses being created that can focus acoustic waves down to small spots [7]. Other applications include acoustic cloaking [8], the acoustic equivalent to invisibility, or thermal isolation, as heat transfers primarily through high frequency vibrations (above 100 GHz) in solid materials [9]. The main focus of such materials is vibration isolation, where an incoming wave is manipulated such that at a specific frequency interval it is attenuated, while leaving waves of other frequencies mostly unaffected.

One area where these acoustic metamaterials could be of particular interest is in the field of levitated mechanics. By magnetically levitating microscopic particles their quantum behaviour can be studied, with a great interest being placed on limits in size and mass for quantum objects [10, 11]. These particles also serve as extremely sensitive sensors of external forces acting on the particle [12–14], with even the gravitational pull between small objects being theoretically measurable with this kind of system. One way to achieve this levitation is through chip-based magnetic traps, where two conducting coils, placed in an anti-Helmholtz configuration, create a magnetic field trapping a superconducting particle via the Meissner effect. Cooling such a system down to low temperatures is essential to its function, with superconductivity a requirement as well as lower ambient thermal noise allowing for more precise and accurate measurements. These low temperatures can be achieved with a dilution refrigerator [15]. A particle situated in such a setup is not only subjected to the ambient thermal noise, but also vibrational noise originating from various sources, from compressors used by the refrigerator to the lab itself. These vibrations drive the motion of the particle, with them contributing to its amplitude to a larger degree than the ambient thermal environment. Meaning if the vibrations ceased the motion of the particle would subside significantly. This noise can be modelled onto the system with an effective temperature given as

$$T_{\mathrm{eff}} = \frac{m\omega^2}{k_{\mathrm{B}}}\langle x^2\rangle, \tag{1.1}$$

where m and x correspond to the mass and displacement of the levitated particle, ω is the angular frequency, and k_{B} is the Boltzmann constant [14, 16]. This means that the effective temperature in the system, which is a measure of the total noise, is proportional to the spread of the particle position $\langle x^2\rangle$. By vibrationally shielding the system this motion can therefore be suppressed. One technique for dealing with this issue is using a mass-spring system to create a low-pass filter for the vibrations, where vibrations corresponding to higher frequencies than the cut-off of the spring system becoming significantly attenuated. However, this creates a problem of its own. As the experimental setup needs to be cooled down to cryogenic temperatures and the spring-system working as a low pass filter, phonons of a higher frequency which are essential for the transfer of heat are attenuated as well [9]. This is a problem which phononic crystals could solve. By creating a band-pass filter instead of a low-pass filter the higher frequency vibrations can be left alone, while vibrations of a lower frequency interval can be suppressed.

1.1 Aims and Objectives

This thesis presents acoustic metamaterials as an alternative method of vibration isolation compared to a mass-spring system for use at cryogenic temperatures. The goal is to of attenuate vibrations at frequencies around 400 Hz without hindering the propagation of high frequency thermal phonons carrying heat. The desired attenuation of this metamaterial is 120 dB, in root-powers, see equation (1.1), with the goal of the particle being thermally driven at low temperatures of 10 mK [14]. In addition to this an experimental setup for measuring the vibrational displacement of these materials has to be developed to characterize the fabricated metamaterials.

This thesis is structured as follows. Chapter 2 presents the underlying theory and background necessary to understand the physics behind acoustic metamaterials, with their function linked to phonons, elastic waves, and certain material properties of solids. Chapter 3 presents the methodology used to design and experimentally characterize the metamaterial, with Chapter 4 presenting the corresponding results. Finally, Chapter 5 presents the final conclusions of the thesis, along with a brief outlook into the future.

2

Theory

In this chapter the underlying theory for this thesis is presented. First the background on phonons, elastic waves, and corresponding material properties is discussed, followed by phononic crystals and metamaterials. Finally, the theoretical background on optical interferometry and homodyne detection is presented.

2.1 Phonons and Elastic Waves

Crystalline solids are materials which have a highly ordered structure on the atomic level, with atoms forming crystal structures known as lattices. Figure 2.1 shows the lattice structures known as face-centred-cubic (FCC) and body-centred-cubic (BCC) in Figures 2.1a and 2.1b respectively. In an FCC structure the atoms are arranged such that they occupy the corners and the centre of each face of the cube. BCC structures, in addition to the atoms in the corners, have a single atom in the centre of the cube itself [17].

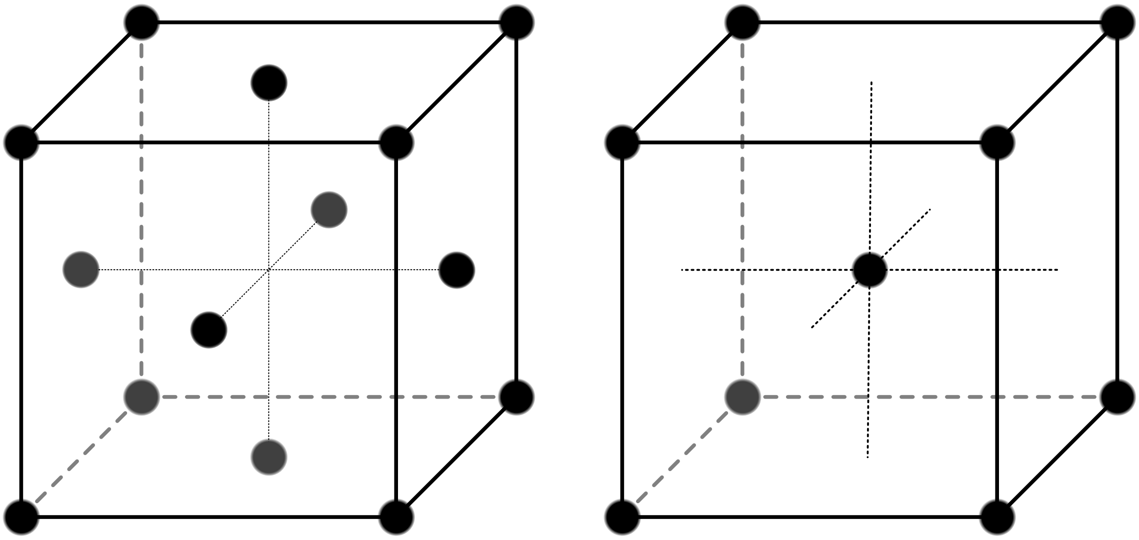

(a) **(b)**

Figure 2.1: In (a) the crystal structure of an FCC lattice. In (b) the crystal structure of a BCC lattice. Atoms for each lattice are marked with black dots with atoms occupying each corner as well.

The crystal structure of these materials is integral to its function and how it can react to its environment. If an ion in a crystalline material is excited by an incoming mechanical energy transfer, for example through a collision, then the resulting motion would propagate throughout the material. This is caused by the strong ion-ion interaction between ions as they repel each other. Meaning a local excitation in the material becomes a collective excitation which can be quantised and referred to as phonons [18]. This concept can then be taken to the macroscopic scale, where the collective excitation of particles is referred to as elastic waves instead.

In general, there are quite a few similarities to draw between light waves and elastic waves. They are described by similar wave equations, and many phenomena associated with light is applicable in a comparable way for phonons. However, one major difference between them is the lack of longitudinal compression in light. As light propagates it is described as a transverse wave, with wave components in vacuum consisting of electric and magnetic fields perpendicular to the direction of propagation. This is not the case for elastic waves, or phonons, where the wave is described as a combination of longitudinal and transverse motion, meaning the vibrations occur both in parallel and perpendicular to the propagation of the wave. This is illustrated in Figure 2.2 where the two types of waves are shown, with a longitudinal and transverse wave in 2.2a and 2.2b, respectively.

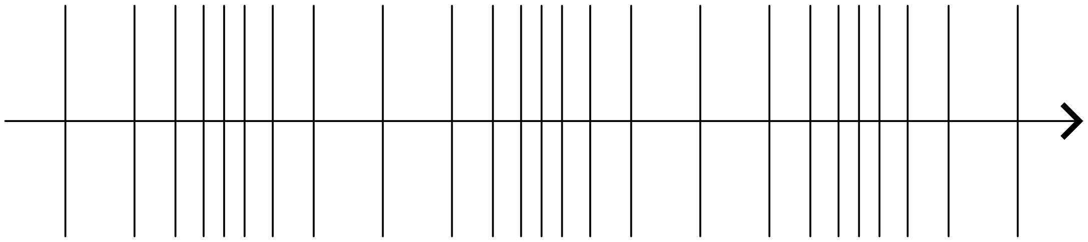

(a)

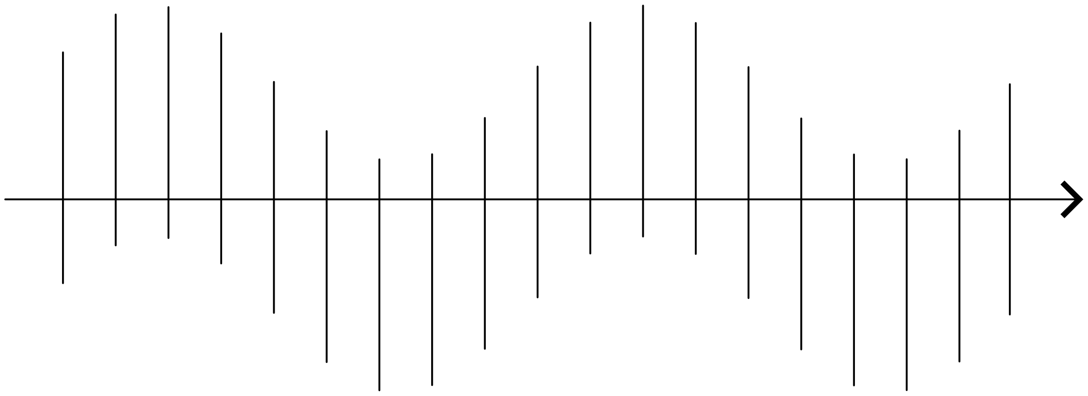

(b)

Figure 2.2: The components of an elastic wave. (a) A longitudinal compression wave where the oscillations of the wave occur in parallel to the propagation of the wave. (b) A transverse wave where the oscillations of the wave occur perpendicular to the propagation of the wave.

The concepts of stress and strain are fundamental in the field of solid mechanics. Stress describes the forces present inside a material when it deforms and strain describes the deformation from its initial stable state. So when a material is deformed it is strained which causes stresses to appear in the material. Stress is generally described in tensor notation with Hooke's law [19] as

$$\boldsymbol{\sigma} = \mathbf{C} : \boldsymbol{\epsilon}, \tag{2.1}$$

where $\mathbf{C}$ is the stiffness matrix, describing the elastic properties of the material, and $\boldsymbol{\epsilon}$ is the strain tensor which is expressed as

$$\boldsymbol{\epsilon} = \frac{1}{2}\left(\boldsymbol{\nabla}\mathbf{u} + (\boldsymbol{\nabla}\mathbf{u})^{\mathrm{T}}\right), \tag{2.2}$$

where $\mathbf{u}$ is displacement. For an isotropic material, i.e., a material that is symmetric with regards to all directions, and concerning only linear deformations, the components of the stiffness tensor can be expressed as

$$\mathrm{C}_{ijk\ell} = \lambda\delta_{\mathrm{ij}}\delta_{\mathrm{k}\ell} + \mu\left(\delta_{\mathrm{ik}}\delta_{\mathrm{j}\ell} + \delta_{\mathrm{i}\ell}\delta_{\mathrm{jk}}\right), \tag{2.3}$$

where μ and λ are the Lamé parameters, and δ_{ij} is the Kronecker delta. The Lamé parameters represent some properties of the material present, which will be discussed further in Section 2.2. The linear equation of motion can be expressed as

$$\boldsymbol{\nabla} \cdot \boldsymbol{\sigma} + \mathbf{f} = \rho\mathbf{a}, \tag{2.4}$$

where $\mathbf{a}$ is the acceleration of the body, $\mathbf{f}$ is an external force per unit volume, ρ is the density, and $\mathbf{a}$ is acceleration. If the strain tensor is rewritten as $\epsilon_{k\ell} = \frac{1}{2}(\partial_\ell u_k + \partial_k u_\ell)$, where ∂_i is the partial derivative, the resulting stress tensor becomes $\sigma_{ij} = 2\mu\epsilon_{ij} + \lambda\epsilon_{kk}\delta_{ij}$. Inserting this into the equation of motion in equation (2.4) results in the wave equation for elastic waves [20] through an isotropic medium as

$$(\lambda + \mu)\boldsymbol{\nabla}\left(\boldsymbol{\nabla} \cdot \mathbf{u}\right) + \mu\nabla^2\mathbf{u} + \mathbf{f} = \rho\partial_t^2\mathbf{u}. \tag{2.5}$$

Assuming there are no forces exerted on the body, i.e. $\mathbf{f} = 0$, equation (2.5) can be used to derive the speed of sound. This is done by first decomposing the wave into purely longitudinal and transverse components. For a purely longitudinal wave the curl of the wave is zero, $\boldsymbol{\nabla} \times \mathbf{u}$. Inserting this into equation (2.5) results in

$$\rho\partial_t^2\mathbf{u} = (\lambda + \mu)\boldsymbol{\nabla}\left(\boldsymbol{\nabla} \cdot \mathbf{u}\right) + \mu\nabla^2\mathbf{u} = (\lambda + 2\mu)\nabla^2\mathbf{u}, \tag{2.6}$$

as $\boldsymbol{\nabla}(\boldsymbol{\nabla} \cdot \mathbf{u}) = \nabla^2\mathbf{u} + \boldsymbol{\nabla} \times (\boldsymbol{\nabla} \times \mathbf{u})$. Similarly, in the case of a purely transverse wave, the divergence of the displacement becomes zero, $\boldsymbol{\nabla} \cdot \mathbf{u} = 0$. Inserting this into equation (2.5) results in

$$\rho\partial_t^2\mathbf{u} = (\lambda + \mu)\boldsymbol{\nabla}(\boldsymbol{\nabla} \cdot \mathbf{u}) + \mu\nabla^2\mathbf{u} = \mu\nabla^2\mathbf{u}. \tag{2.7}$$

Here, the propagation speed inside an isotropic material is given as

$$c_\ell = \sqrt{\frac{\lambda + 2\mu}{\rho}}, \qquad c_{\mathrm{t}} = \sqrt{\frac{\mu}{\rho}}, \tag{2.8}$$

where c_ℓ and c_{t} are the longitudinal and transverse speeds of sound, respectively.

2.1.1 The Brillouin Zone

A standard way to model the characteristics and properties of a periodic medium is through the first Brillouin zone, commonly referred to as just the Brillouin zone. This is a uniquely defined area in the reciprocal space of a lattice, which describes the Fourier transform of the positional lattice, see Figure 2.1 for an example of such a lattice. The Brillouin zone is a primitive cell of the reciprocal space, as it tessellates the space, and is used to describe the propagation of waves in such materials. Figure 2.3 shows the Brillouin zone in the reciprocal space, corresponding to a square lattice in real space. These reciprocal lattice points correspond to wave vectors of plane waves with the shaded region representing the Brillouin zone.

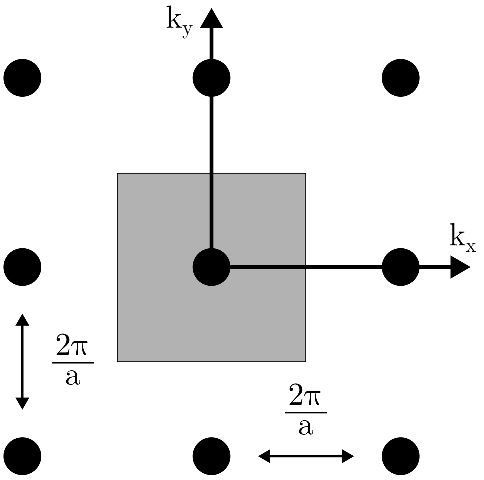

Figure 2.3: Illustration of the Brillouin zone in the reciprocal space for a square lattice with lattice constant a. Dots correspond to wave vectors with the shaded region representing the Brillouin zone.

Because of the periodicity of the medium studied this Brillouin zone contains enough information of the system to describe it in its entirety, with information corresponding to higher wavelengths being folded back into the Brillouin zone [21]. Figure 2.4 shows an example of a square lattice, where the so-called high symmetry points Γ, X, and M correspond to wave vectors $\mathbf{k} = (\mathrm{k}_x, \mathrm{k}_y)$: (0, 0), $(\pi/a, 0)$, and $(\pi/a, \pi/a)$, respectively, with the lattice constant a. The area between these points is known as the irreducible Brillouin zone. For example, a wave propagating along Γ to X results in a wave purely along the x-axis, as $\mathrm{k}_y = 0$, while between the Γ- and M-point the wave would be travelling along both x- and y-axis with the same magnitude. At the centre of the zone, at Γ, the wave vector becomes zero, i.e., $\mathbf{k} = 0$, meaning the wavelength of the wave becomes infinite, as $\mathrm{k} = 2\pi/\lambda$. This is known as the long wavelength limit, which means the lattice starts behaving as a single material as the wavelength is much larger than any geometry associated with the cells or atoms of the lattice. In contrast, at the edge of the Brillouin zone the wavelength of the wave becomes twice the lattice constant, $\lambda = 2a$. At these points a phenomenon known as Bragg scattering occurs which will be discussed further in Section 2.3.1.

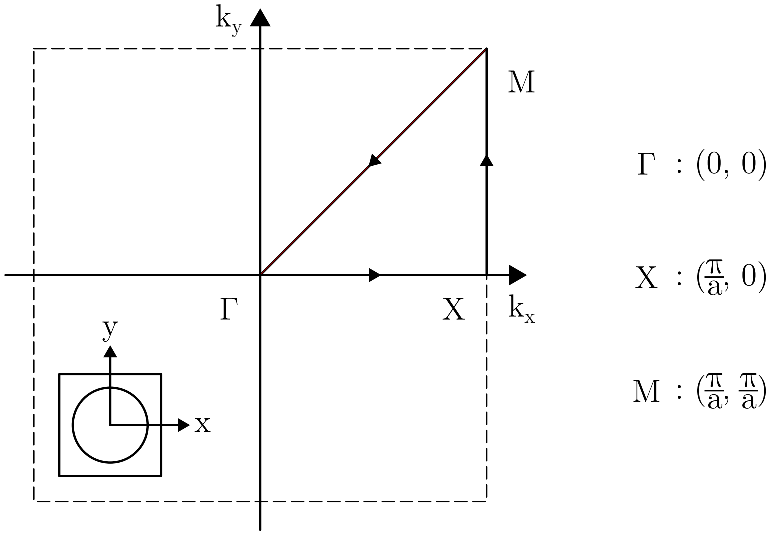

Figure 2.4: The first Brillouin zone of a simple square lattice. The three high-symmetry points of this lattice are shown at the points Γ, X, and M, corresponding to wave vectors as shown to the right, where a is the lattice constant, together composing the irreducible Brillouin zone.

2.1.2 The Dispersion Relation

The propagation of waves through a periodic structure can be described by the dispersion relation of the wave [21]. The dispersion relates the wavelength of a wave to its frequency through the velocity of propagation, whose speed is calculated through the slope of this relation, with the group and phase velocities of a wave defined as

$$v_g = \frac{\partial \omega}{\partial k}, \qquad v_p = \frac{\omega}{k}, \tag{2.9}$$

where ω, k is the angular frequency and wave vector, respectively. Figure 2.5 shows the dispersion relation of copper, in a square lattice with lattice constant a, with the points Γ, X, and M. The bands in the dispersion relation represents the vibrational modes of the phonons, with each band corresponding to a different mode of vibration. For example, one band might represent an in-phase vibration, where everything oscillates in-phase, whereas another band might represent an out-of-phase oscillation. In particular, the bands originating at the Γ-point are known as the acoustic bands. These bands describe the in-phase vibrational modes of the lattice, whose slopes at $k \to 0$ is the definition of the speed of sound of a material. There being multiple slopes leads to multiple definitions of the speed of sound, corresponding to longitudinal and transverse speeds, as discussed in section 2.1. In general, there are a number of acoustic modes equal to the number of dimension observed, with each dimensions introducing a direction of motion with oscillations in x-, y-, and z-directions. The remaining bands are called optical bands, and represent the out-of-phase oscillations of the lattice.

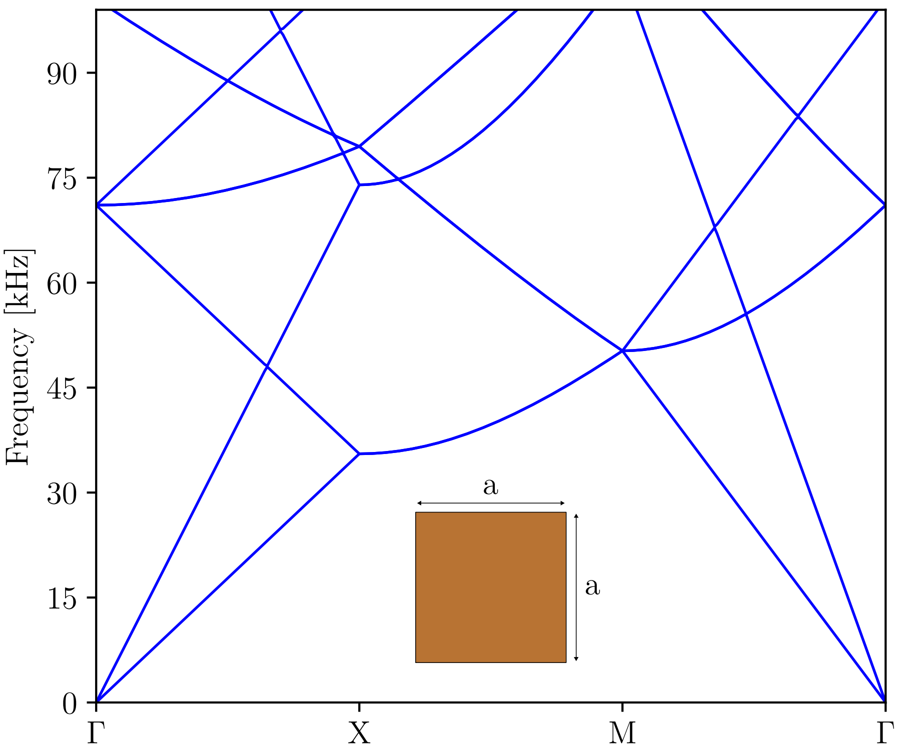

Figure 2.5: Dispersion relation for copper (bottom) in two dimensions with the frequency shown as a function of the lattice wave vector with the resulting bands describing the vibrational modes of a propagating wave.

2.2 Mechanical Properties of Solids

As shown in equation (2.8) the propagation speed of a wave is dependent on mechanical properties of the propagation medium. The Lamé parameters are representations of these properties, with μ describing the shear modulus, which is one of many elastic moduli of a material. The other Lamé parameter, λ, does not have a direct physical interpretation and is instead used to describe other properties, with

$$\lambda = K - \frac{2}{3}\mu, \tag{2.10}$$

where K is the bulk modulus, which is a measure on volumetric compressibility. These moduli describe the relation between stress and strain in a specified direction and make up the stiffness tensor in an isotropic material, as presented in Section 2.1. The moduli are defined as the slopes of the linear region of the strain-stress relationship [19], where deformation is reversible meaning the material is elastic, in contrast to the plastic region of a material, where deformation becomes permanent. In this thesis only linear elasticity will be concerned for isotropic materials, meaning the elastic moduli are presented as scalar values. This results in the shear modulus

$$\mu = \frac{\sigma_{\text{shear}}}{\epsilon_{\text{shear}}}, \tag{2.11}$$

where σ_{shear} and ϵ_{shear} represent shear stress and strain, respectively. The corresponding moduli for longitudinal, or axial, tension becomes

$$E = \frac{\sigma_{\text{axial}}}{\epsilon_{\text{axial}}}, \tag{2.12}$$

and is referred to as the Young's modulus.

Another important material property is the Poisson ratio, which describes the relation between the axial and transverse strains of a material, i.e., how much the material expands horizontally when subjected to a vertical deformation. This ratio is given as

$$\nu = \frac{\epsilon_{\text{trans}}}{\epsilon_{\text{axial}}}, \tag{2.13}$$

where ϵ_{trans}, and ϵ_{axial} are the material strains in the transverse, and longitudinal directions, respectively [22]. This concept is illustrated in Figure 2.6 where axial tension, shown with a pressure P, on a material (left) results in axial elongation and horizontal contraction of a conventional material (centre) with a positive Poisson ratio. Most naturally occurring materials have a positive Poisson ratio [23], with 0.5 being the highest allowed, occurring in soft materials like silicone rubber as well as fluids, as they are incompressible. Materials exhibiting a Poisson ratio of close to zero are, for example, porous materials such as cork, where axial compression does not affect its horizontal elongation much. A negative Poisson ratio, on the other hand, would result in, for example, horizontal expansion during axial tension. Materials such as these are known as auxetic [22, 23], an example of which is shown in Figure 2.6 (right), where a similar axial elongation as for the conventional material is observed, however, with a horizontal elongation as well.

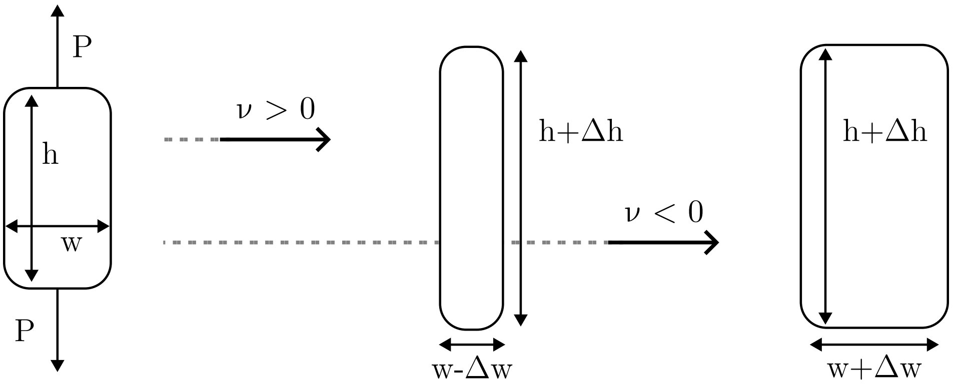

Figure 2.6: Illustration of the Poisson ratio. (Left) A material being subjected to axial tension by pressure P, with the response of a material with a positive ν (centre) and a material with a negative ν (right).

The two above mentioned quantities, E and ν, along with the density of a material, allow for most elastic interactions within an isotropic material to be explained. As stated earlier the Lamé parameters can be used to the same end, however, since λ is not as rooted in an observable quantity, they will not be used going forward and instead be rewritten in terms of E and ν [19]:

$$\mu = \frac{E}{2(1+\nu)}, \qquad \lambda = \frac{E\nu}{(1+\nu)(1-2\nu)}. \tag{2.14}$$

Inserting equation (2.14) into equation equation (2.8) allows the speed of sound to be expressed as a function of Young's modulus and the Poisson ratio as

$$c_\ell = \sqrt{\frac{E(1-\nu)}{\rho(1+\nu)(1-2\nu)}}, \qquad c_\mathrm{t} = \sqrt{\frac{E}{2\rho(1+\nu)}}, \tag{2.15}$$

meaning that the speed of sound inside a material becomes larger with a stiffer material, corresponding to a higher Young's modulus.

2.2.1 Solids at Cryogenic Temperatures

In general, the environment will have significant effects on material properties. For example, high temperatures can lead to materials losing key features, such as their magnetization if they exceed their Curie temperature [24]. A very cold environment can cause similar effects, with certain materials becoming superconducting at sufficiently low temperatures, becoming perfect electrical conductors with zero resistance and their thermal conductivity dropping significantly [25]. A more relevant property that is also affected by low temperatures is material stiffness. The stiffness of a material will generally rise with decreased temperatures, meaning elastic moduli such as Young's modulus or the shear modulus will increase [26, 27]. This means the materials become more brittle, meaning they are more likely to shatter or break when subjected to external forces rather than elongate elastically. The Poisson ratio behaves a bit differently at low temperatures, with it not varying by large amounts even at cryogenic temperatures. This is due to the fact that it is dependent on a ratio between the Young's modulus and the shear modulus and since both of them increase similarly, the ratio remains mostly temperature independent.

Another consequence of low temperatures is thermal expansion. Generally, as temperature drops materials will contract, with certain types of materials being affected more than others. For example, metals, like copper and aluminium, undergo much less thermal contraction than polymers and glasses. There are also materials for which this is not the case, with their thermal expansion coefficient, a measure of the thermal expansion, exhibiting a minimum at temperatures above absolute zero. An example of this is single-crystal silicon, whose thermal coefficient hits a minimum at about 80 K and then grows with decreasing temperature [28]. Figure 2.7 shows an illustration of this phenomenon, where the thermal coefficient is shown as a function of temperature, with a global minimum at a temperature above absolute zero and a rising thermal coefficient at temperatures below the minimum.

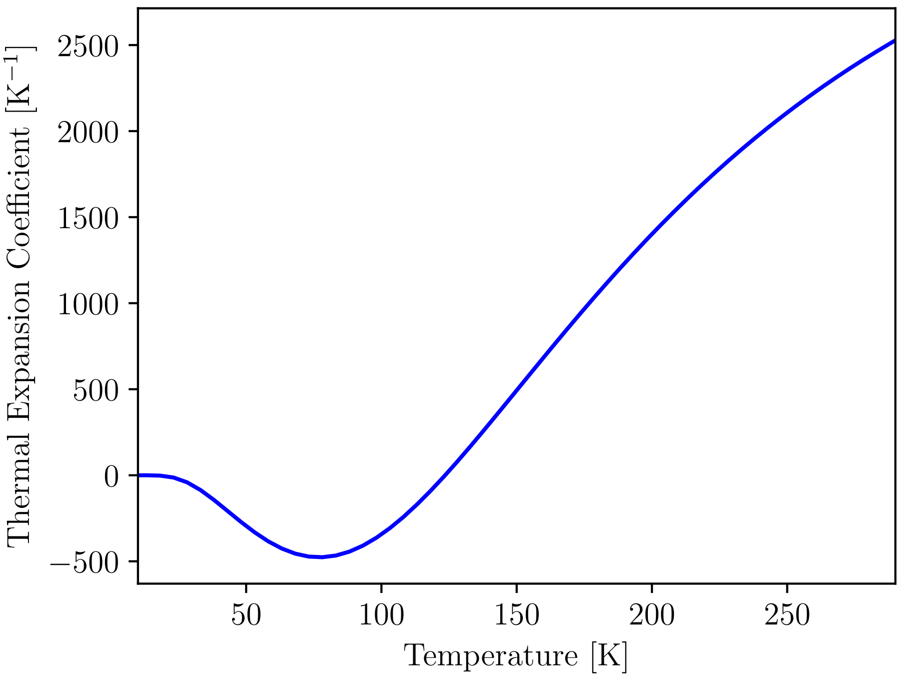

Figure 2.7: Thermal expansion coefficient for single-crystal silicon as a function of temperature [28]. A negative dip in the coefficient can be observed at around 80 K, with it approaching zero as temperature decreases further.

2.3 Phononic Crystals and Metamaterials

Phononic crystals are materials which are engineered to manipulate and control elastic waves in solids in ways that are not possible with conventional materials. These wave modifications usually come in the form of attenuation of waves propagating with certain frequencies, but they can also be used to, for example, guide acoustic waves along a specified path [29], like a waveguide for electromagnetic waves. An example of a phononic crystal in action can be seen in Figure 2.8 where an incoming

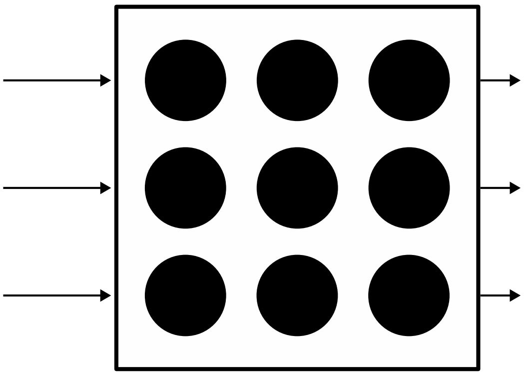

Figure 2.8: Illustration of the effects a phononic crystal can have on an incoming excitation, here in the form of a pressure wave, with the transmitted signal being attenuated due to the inclusions placed into the material.

pressure wave is attenuated by an array of cylindrical voids inside a host material, represented with the outgoing arrows becoming smaller. This attenuation can be controlled in such a way that a specific frequency interval is targeted, meaning any wave of a frequency outside of the desired region is unaffected. This corresponds to a band-stop filter in electronics, with both lower and higher frequencies being ignored. The attenuated waves are then either reflected back or absorbed as energy into the material. These band-stops are known as band gaps and are mainly generated by two different mechanisms: either through Bragg scattering, or localised resonances, to be discussed in Sections 2.3.1 and 2.3.2, respectively.

A way to visualize the differences between the phononic crystal and a bulk material is to look at its dispersion relation. As seen in Figure 2.5 the dispersion relation for such a bulk material, of copper, is made up of many bands, with no frequency interval where no band can be found, meaning no band gaps and phonon propagation being allowed at all frequencies. This is not the case for a phononic crystal. Figure 2.9 shows the dispersion relation for an identical copper sample with a lattice constant $a = 3$ cm, however, with a circular void with diameter $b = 2.7$ cm at its centre. This void leads to the generation of a band gap at frequencies of 36–51 kHz where there are no available phononic modes. This specific type of band gap is

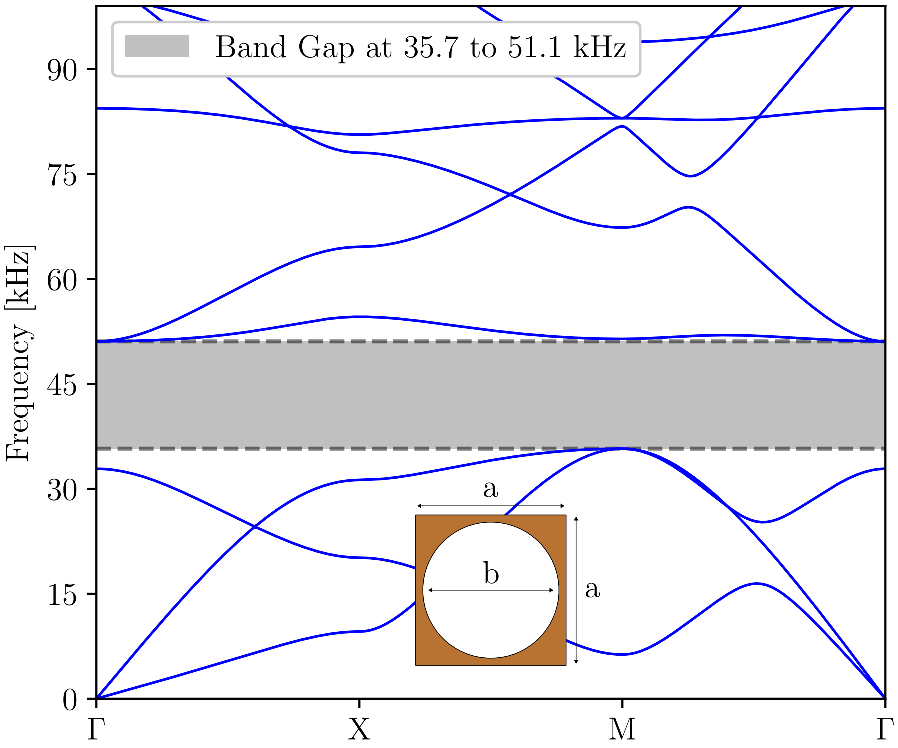

Figure 2.9: Dispersion for a copper phononic crystal (bottom) in two dimensions with the frequency shown as a function of the lattice wave vector. This dispersion relation is calculated for an infinite two-dimensional array of the unit cell. At frequencies of 35.7–51.1 kHz a complete band gap can be seen, where phonon propagation is forbidden.

known as a complete band gap as opposed to a directional band gap, where only a partial band gap can be found at some paths. For example, a directional band gap could be obtained where there is a band gap between Γ and X, but at all other paths there is at least one mode available. This would mean that any wave travelling along the x-axis would be attenuated in an infinite array of cells. Directional band gaps can for example be used to create directional filters with phononic crystals, where, for example, only waves from a specific direction are attenuated, while the rest are able to propagate. In a finite situation this might not be the case, as the dispersion relation is calculated for an infinite array of unit cells.

Thermal phonons are an important factor in determining the thermal conductivity of a material. As phononic crystals are created with the aim of suppressing phonons from propagating this can cause thermal conductivity to become lower as well. However, if the wavelength of these phonons is much smaller than the phononic crystal it will not affect them. At that scale the wave will only see the material in its path, the features that lead to the band gaps of the phononic crystals are too big to affect the phonons. Essentially as long as the phononic crystal is not designed in such a way to attenuate the frequencies of thermal phonons they will not be affected by it.

2.3.1 Bragg Scattering

In general, the main method used to open up band gaps is based on Bragg scattering. This concept is based on the scattering that occurs as a wave interacts with a periodic medium. For example, periodic inclusions or voids, see Figure 2.9, where a periodic disturbance to the material has been added. This effect is especially important at the edge of the Brillouin zone, where k= π/a, where the wavelength λ is twice the lattice constant a. At these points the reflections and scattering lead to the interference of consecutive reflected and forward propagated waves since the neighbouring cells are oscillating completely out-of-phase. This leads to standing waves forming and forward propagation of the wave being inhibited, meaning an effective band gap has formed at these wavelengths [30].

These band gaps form at wavelengths $\lambda = 2a$, i.e., at frequencies $f = c/2a$, where c is the propagation speed of the wave, as wave propagation in the forward direction is of most interest the longitudinal speed of sound is used. This becomes an issue if the targeted frequency interval is placed too low, as unit cell spacing could become too large. For example, if the aim is to create a band gap of 500 Hz or 5000 Hz with copper, which has a speed of sound on the order of $5 \cdot 10^3$ ms^{-1} [31], a lattice constant a on the order of 1 metre to 10 metres would be required, something which is not suitable for the targets of this thesis.

2.3.2 Local Resonance

Band gap generation via localised resonance is a method in which local resonances are created inside the phononic crystal which can lead to the creation of band gaps. This method is not limited to the size of the phononic crystal as these resonances can be created within the unit cells themselves. Materials which achieve this are called acoustic metamaterials, materials whose properties are tied to their structure rather than size or composition and which affect phenomena with corresponding wavelengths that are larger than the periodicity of themselves. These qualities can be achieved by, for example, introducing resonant features inside the unit cell of an already existing phononic crystal. As the wavelengths targeted are larger than the unit cell size, smaller details present inside the cells, such as other inclusions or patterns, starts becoming invisible to the wave. This is most true at the long wavelength limit, but the effect gradually betters as the wavelength increases. As this happens the wave sees the structure as an effective material, meaning any local resonances caused by the smaller features can cause changes in this effective structure. Then material properties like effective mass or elasticity can be modified locally to create dynamic effective parameters that do not normally exist in conventional materials.

A simple material property to modify is the mass density. If the mass density of the material were to drop below zero then the propagation speed becomes imaginary, see equation (2.15). This is an effect typically associated with evanescent waves, i.e., waves that decay exponentially as they propagate. Essentially what this means is that as the elastic waves attempt to propagate through the material they will lose their energy and die out.

This negative effective mass can be achieved with local resonances and a simple analogue can be found in a mass-spring system. Figure 2.10 shows a system in which a mass m is connected to another mass M via a spring k. Assuming this system is subjected to an external force F the equations of motion are

$$\begin{cases} m\ddot{u}(t) = -k(u(t) - U(t)) \\ M\ddot{U}(t) = -k(U(t) - u(t)) + F(t) \end{cases} \tag{2.16}$$

where u and U represent the displacement of the inner and outer masses, respectively. This can then be solved as a harmonic solution by using Fourier transform as

$$F(\omega) = -\omega^2 \left(M + \frac{\omega_0^2 m}{\omega_0^2 - \omega^2} \right) U(\omega) = M_{\text{eff}}(\omega) \cdot \left(-\omega^2 U(\omega) \right), \tag{2.17}$$

where $\omega_0^2 = k/m$, and M_{eff} is the resulting dynamic effective mass of the system. This effective mass is shown in Figure 2.10 as a function of frequency. A region of negative mass can be observed at frequencies of 100–141 Hz, with $m = M = 1$ kg and $\omega_0 = 100$ Hz. A negative effective mass effectively means that if subjected to an external force it would accelerate against it. This kind of structure can be replicated without the use of conventional springs. By using solids with high elasticity the effect of these springs can be emulated [1, 32].

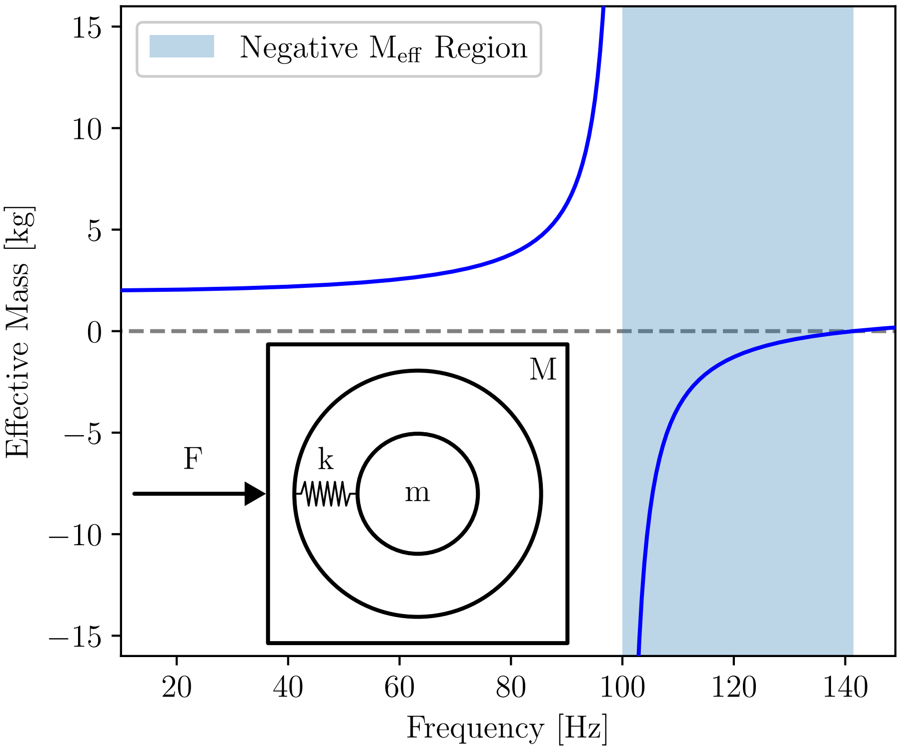

Figure 2.10: The effective mass of the mass-spring system (bottom left) as a function of frequency, where a region of negative mass can be observed at frequencies of 100–140 Hz.

A negative effective Young's modulus would have a similar effect as the density modulation as the propagation speed of the wave would become imaginary. In effect, a negative Young's modulus would cause the material to elongate when compressed or shorten when stretched. This is most commonly used in the field of acoustics. For example, an attached Helmholtz resonator to a pressure chamber can cause the compressibility of the chamber to become dynamic, and become negative at certain frequencies [32, 33]. This is specifically of great use with gases as they are highly compressible, unlike solids and fluids.

Finally, there is the option to have both a negative effective mass density and elastic modulus. If these effective parameters are both negative in the same frequency interval the propagation speed becomes real. This means no forbidden region for the propagating wave and thus no band gap generation. However, if they were to become negative at different intervals the resulting metamaterial would have multiple band gap regions. One interesting consequence of a double negative metamaterial [34] is the effect it has on the phase velocity of the wave. In a double negative metamaterial the phase velocity becomes negative instead, with an effect similar to negative refraction occurring for the elastic waves [35] where light is refracted opposite the expected direction. If these parameters become negative at different intervals the metamaterial would simply have multiple coexisting band gaps at the different frequency intervals.

2.4 Interferometric Vibration Sensing

To characterize an acoustic metamaterial, a quantity that can be studied is the transmission of vibrations through the material. By comparing the displacement of an incoming excitation against the displacements at the other end of the material the attenuation caused by the metamaterial can be calculated as the ratio between the two. A simple setup of this is shown in Figure 2.11 where an incoming excitation, $u_0(t)$, is sent to the base of the metamaterial with the transmitted signal, $u_1(t)$, measured at the end of it.

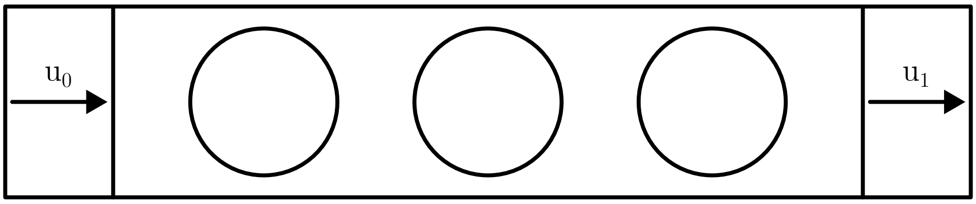

Figure 2.11: Setup to measure the transmission of displacement for an acoustic metamaterial with u_0 and u_1 representing the displacement at the base and the end of the total sample, respectively.

There exists a few ways to solve this problem with methods such as placing the sample between two piezoelectric transducers and measuring the voltage over each as one end is excited. However, in this thesis the focus will be placed on optical interferometry as the method can be generally applied to low temperature environments as well. More specifically balanced homodyne detection was used. Homodyne detection allows for information to be extracted from a modulated signal, for example the phase modulation caused by a shifting optical path length, by referencing it to a stable known signal. Figure 2.12 shows a simple overview of a homodyne detection system where a laser beam is first shown splitting into two arms, the local oscillator (LO) and the signal arm. The LO arm acts as the reference, an unmodulated signal, while the signal arm is modulated along its path. These signals then interfere at a final beam splitter, producing two signals which can be subtracted from one another to obtain a DC signal proportional to the signal modulation.
Where the homodyne system sets itself apart is with its ability to produce a high signal to noise ratio. The amplitude of the signal arm can be described by

$$\alpha_s(t) = \alpha_s + \delta X_s(t) + i\delta Y_s(t), \tag{2.18}$$

where α_s is a steady-state amplitude, and $\delta X_s(t)$ and $\delta Y_s(t)$ are the amplitude and phase quadratures of the signal arm respectively [36]. These quadratures are real numbers which describe the fluctuations of the laser beam. In the same way the LO arm can be described by

$$\alpha_{\mathrm{LO}}(t) = (\alpha_{\mathrm{LO}} + \delta X_{\mathrm{LO}}(t) + i\delta Y_{\mathrm{LO}}(t)) \cdot \exp(i\varphi), \tag{2.19}$$

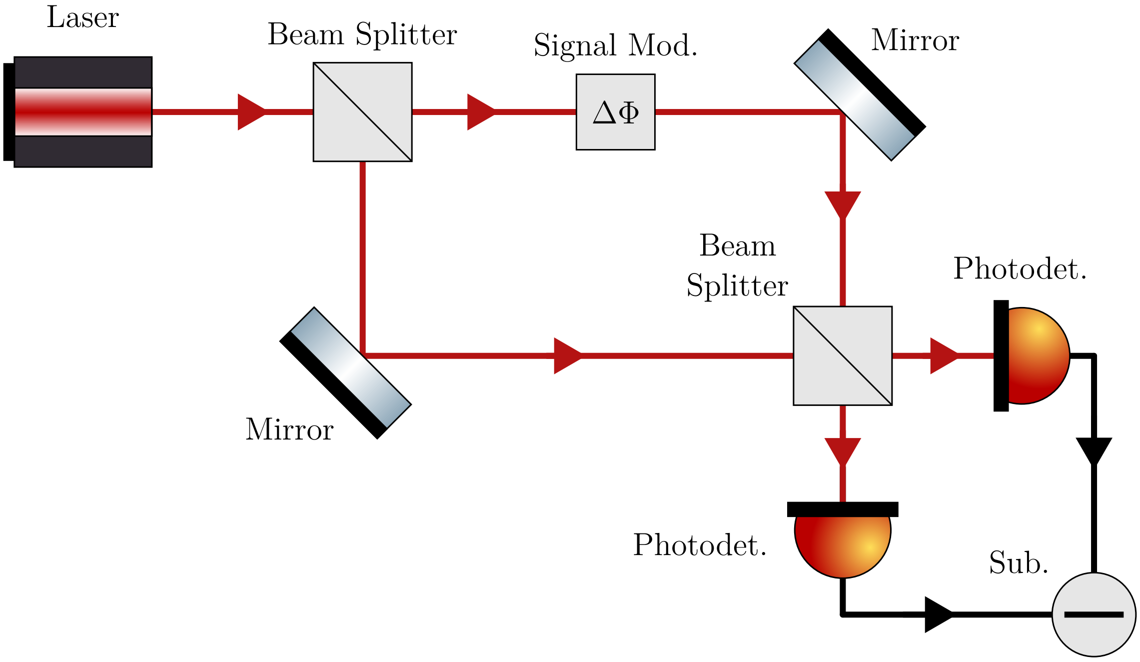

Figure 2.12: Overview of a homodyne detection setup where a laser is guided through two arms, one arm being modulated, and into a final beam splitter to interfere, producing a signal that can be analysed to determine the signal modulation.

where φ is the relative phase between the LO and signal arms. A 50:50 beam splitter can be modelled according to

$$T = \frac{1}{\sqrt{2}} \begin{bmatrix} 1 & 1 \\ 1 & -1 \end{bmatrix}, \tag{2.20}$$

which results in the combination of the LO and signal arm as

$$T \begin{bmatrix} \alpha_s(t) \\ \alpha_{\mathrm{LO}}(t) \end{bmatrix} = \frac{1}{\sqrt{2}} \begin{bmatrix} \alpha_s(t) + \alpha_{\mathrm{LO}}(t) \\ \alpha_s(t) - \alpha_{\mathrm{LO}}(t) \end{bmatrix} \equiv \begin{bmatrix} \alpha_1(t) \\ \alpha_2(t) \end{bmatrix}. \tag{2.21}$$

The intensity of a beam is given by the absolute square of the field meaning the two beams presented in equation (2.21) produce intensities according to

$$I_1(t) = |\alpha_1(t)|^2 = \frac{1}{2}\left(|\alpha_s(t)|^2 + |\alpha_{\mathrm{LO}}(t)|^2 + \alpha_s(t)\alpha^*_{\mathrm{LO}}(t) + \alpha^*_s(t)\alpha_{\mathrm{LO}}(t)\right) \tag{2.22}$$

$$I_2(t) = |\alpha_2(t)|^2 = \frac{1}{2}\left(|\alpha_s(t)|^2 + |\alpha_{\mathrm{LO}}(t)|^2 - \alpha_s(t)\alpha^*_{\mathrm{LO}}(t) - \alpha^*_s(t)\alpha_{\mathrm{LO}}(t)\right). \tag{2.23}$$

If second order terms of the fluctuations, i.e. $\delta X_s(t)\delta X_{\mathrm{LO}}(t)$, are disregarded as the fluctuations are assumed to be tiny, the resulting intensity of the homodyne signal, which is equal to the difference between the intensities in equations (2.22) and (2.23), becomes

$$\begin{aligned} I_{\text{homod.}} = {} & 2\alpha_s\alpha_{\text{LO}}\cos\varphi + 2\alpha_{\text{LO}}\left(\delta X_s(t)\cos\varphi + \delta Y_s(t)\sin\varphi\right) + \\ & + 2\alpha_s\left(\delta X_{\text{LO}}(t)\cos\varphi - \delta Y_{\text{LO}}(t)\sin\varphi\right). \end{aligned} \tag{2.24}$$

Using the phase φ the formulation of the intensity of the homodyne signal means that the measured quadrature of the system can be chosen. For example, if the desired quadrature is the phase quadrature the relative phase can be set to $\varphi = \pi/2 + n\pi$, where $n \in \mathbb{R}$, meaning equation (2.24) becomes

$$I_{\text{homod.}} = 2\alpha_{\text{LO}}\delta Y_s(t) - 2\alpha_s\delta Y_{\text{LO}}(t), \tag{2.25}$$

where now the amplitude ratio between the signal and LO arms can be chosen as $|\alpha_{\text{LO}}| \gg |\alpha_s|$ meaning the final homodyne signal becomes

$$I_{\text{homod.}} = 2\alpha_{\text{LO}}\delta Y_s(t). \tag{2.26}$$

The same could be done for the amplitude quadrature by letting $\varphi = \pi + n\pi$.

The intensities shown in equations (2.22) and (2.23) can then be expanded further, under the assumption $|\alpha_{\text{LO}}| \gg |\alpha_s|$, according to

$$I_1(t) = \frac{1}{2}\alpha_{\text{LO}}^2 + \alpha_{\text{LO}}\delta X_{\text{LO}}(t) + \alpha_{\text{LO}}\left[(\alpha_s + \delta X_s(t))\cos\varphi + \delta Y_s(t)\sin\varphi\right] \tag{2.27}$$

$$I_2(t) = \frac{1}{2}\alpha_{\text{LO}}^2 + \alpha_{\text{LO}}\delta X_{\text{LO}}(t) - \alpha_{\text{LO}}\left[(\alpha_s + \delta X_s(t))\cos\varphi + \delta Y_s(t)\sin\varphi\right]. \tag{2.28}$$

The intensities shown in equations 2.27 and 2.28 can be used to select the desired quadrature when implementing this experimentally, this will be further discussed in Section 3.2.3.

3

Methods

In this chapter the methodology for the three main parts of this thesis is presented: the design and simulation of the metamaterial, the experimental setup used for characterization of the samples, and the process of characterization of the fabricated samples with phase locking and calibration of the setup described.

3.1 Design and Simulation

In this section an overview of the design process is presented along with a description of the physics simulations performed to calculate the dispersion relation and transmission spectra for the metamaterial.

3.1.1 Design Process and Fabrication

The three main considerations when designing the acoustic metamaterials were: physical dimensions, the choice of materials, and the geometry and shape of both its internal and external structures. Limitations were placed on the dimensions of the metamaterials, meaning both the number of cells and the size of the cells themselves were constrained, as the physical limitations of what could fit inside the cryostat were on the order of 10 cm. As stated in Section 2.3 the number of unit cells affect the total attenuation of the PnC, as well as how closely its transmission spectrum lines up with the dispersion relation of the corresponding unit cell. However, the size of the unit cell also affects the location of any potential band gaps in frequency space, with a smaller cell resulting in a band gap at a higher frequency and vice versa. This results in a trade-off: smaller cells for greater attenuation or larger cells for a band gap at lower frequencies.

The second consideration came in the form of the internal and external structure of the PnC. The first choice to be made here is the decision between working in two or three dimensions. In general, working in three dimensions allows for more flexibility as there is simply more room to work with. Conversely, two dimensions could be sufficient for situations where the goal is simply to attenuate a wave that is primarily propagating in one direction. In this case the option chosen was two dimensions, as attenuation is only required along one axis as well as to allow for simpler fabrication. Limiting the dimensions to one dimension is too strict, leaving material contrasts as the only way to periodically modify the metamaterial, as is the case with a one-dimensional superlattice, i.e., periodic layers of two or more materials. Then comes the question of creating a metamaterial band gap, i.e. how to achieve either a negative effective mass density or elasticity modulus, as discussed in Section 2.3.2. Essentially, this comes down to whatever option is easier to realise in fabrication and with the aspect of working with acoustic waves in solids as opposed to fluids. In general, the concept of a negative effective elasticity modulus is more commonly related to attenuating waves in fluids, where the fluid is diverted into smaller chambers along a primary path [32, 33].

Finally, the matter of material composition where there are essentially two options available, either a single phase structure, consisting only of one material, or a composite structure, consisting of multiple distinct materials. A composite structure would allow for greater flexibility in design, creating material contrasts which could affect the elastic waves similarly to how impedance mismatching can create reflections in electric circuits [37]. Another advantage of using multiple materials could be, for example, introducing a heavy element into a lighter frame to affect the resonance of a local resonator type metamaterial, see Section 2.3.2. If the central mass in Figure 2.10 was raised it would lead to a lower resonant frequency, as $\omega_0^2 = k/m$ would be lowered. However, in reality fabrication will play a role in this decision. When joining different materials certain faults or irregularities could arise that would not be a concern for single phase structures. This is especially a concern when discussing applications in a low temperature environment, with different materials, for example, thermally expanding at different rates. This could cause issues with stress and strain inside the structure meaning it might not behave as expected, potentially leading to fractures between materials or permanent plastic deformations.

The fabrication consisted of using laser cutting to cut out two dimensional shapes out of a bulk material, a method in which a high power laser vaporizes the material in order to remove it [38]. There is one major downside to laser cutting as a method, if the sample has individual parts that are too thin they can deform under the heat of the laser, meaning they might not obtain their desired shape as they deform. These imperfections limit the size of certain features, e.g. thin connections or smaller features, meaning certain adjustments from optimal simulated results might need to be made to ensure a functioning sample. An alternative to this is to use 3D printing where the material is simply extruded into layers which are stacked vertically on top of one another. This will, however, lead to the structure not being as homogeneous, meaning that the structure might not behave as expected.

3.1.2 Physics Simulation

The method chosen to simulate the physics behind the solid mechanics of the problem is the finite element method, FEM [39]. This is a process in which problems are discretized into a finite number of smaller elements, with simpler geometries, whose differential equations can be solved numerically. Figure 3.1 shows this discretization in action, for both the unit cell (left) and the complete sample (right), which was performed with COMSOL Multiphysics® [40]. Here the division of the structure is made up from many small triangles which span the surface, in x- and y-directions, and divide up any separate areas, either because of material contrasts or geometric boundaries. This method is often employed in situations where the underlying equations do not have a simple analytical solution and become too complicated to solve otherwise. COMSOL is one such software which is capable of performing these calculations. It uses an extensive library of tools and physics models to accurately simulate a given scenario and is used in this thesis to model both the dispersion relation and transmission spectra for the studied samples.

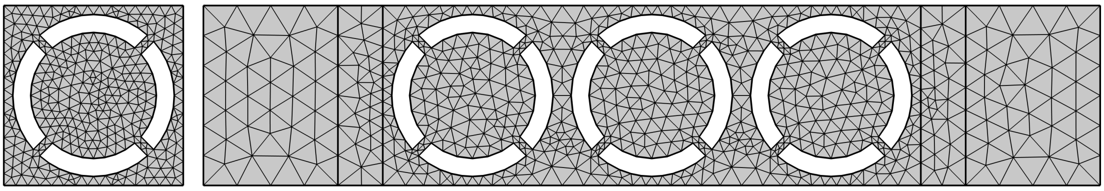

Figure 3.1: Discretized samples for both the unit cell (left) and complete sample (right) with meshing from COMSOL.

To simulate the dispersion relation for a given unit cell an infinite two-dimensional array, in both x- and y-directions, of the cells are studied in COMSOL. This is done to accurately model the material, where an infinite array results in a better representation of its qualities than otherwise. At the boundaries between each cell, boundary conditions are defined via Floquet boundaries, where the wave vector is assigned periodically per unit cell and corresponding high symmetry point in the irreducible Brillouin zone, as discussed in Section 2.1.1. These symmetry points are swept from Γ to X to M to Γ, as to ensure that every possible path is covered, and the rest can be inferred by symmetry. If the unit cell in question was non-symmetric, i.e., the irreducible Brillouin zone would not cover every unique path, then either the entire first Brillouin zone or another symmetric region would have to be studied instead. The omission of any spanning of the cell in the vertical direction is caused by the isotropic nature of the samples shown, where any wave incident perpendicular to the surface of the two dimensional sample will interact with a bulk material.

Simulating the transmission spectra for a sample is done similarly as for the dispersion relation, however, with a finite sample. The simulated sample is made up of a finite array of the aforementioned unit cells, with an excitation being sent along the axis of interest. The displacement caused by this excitation is thereafter extracted from the simulation at both the base and end of the sample, with the resulting ratio of the two describing how much of the wave has been transmitted through the sample. This is performed at a range of frequencies, depending on the obtained dispersion relation, in order to acquire a transmission spectra. In theory, at frequencies corresponding to band gaps in the dispersion relation dips in the transmission should be visible. If the band gap is directional this is only the case if the excitation occurs in a direction where a band gap is predicted. If there are no visible dips, then the number of unit cells is not high enough to accurately capture the characteristics of the unit cell, with an increasing amount of unit cells leading to a better representation of the calculated dispersion relation.

3.2 Characterization of Samples

The method with which to characterize the fabricated devices was based on measuring the displacement using optical interferometry. Specifically, balanced homodyne detection was used to this end. The displacement of the metamaterial was thereafter compared to a corresponding sample of a bulk material in order to calculate the attenuation caused by the metamaterial. In order to calculate this displacement the optical system needs to be calibrated as well, i.e. the signal output needs to be related to the motion measured.

3.2.1 Experimental Setup

The experimental setup used for the balanced homodyne detection system is shown in Figure 3.2. The main goal of this setup is to correlate the output signal to the signal modulation caused by the motion of a vibrating resonator. The resulting signal is presented in equation (2.24) where the intensity is proportional to the phase quadrature if the setup can be locked to the correct relative phase φ, as discussed in Section 2.4. Most of this setup is based on fibre-optics, with every part except for the signal modulation being connected through it while the setup for the signal modulation is based on free-space components. This results in greater flexibility and ease of alignment as fibre-optical components are simply connected to one another. First a laser[1] with a wavelength of 1550 nm is sent through a beam splitter[2], splitting the beams into two parts: the signal arm and the LO arm. The beams are split with a coupling ratio of 90:10, with 90% and 10% sent through the LO and signal arm, respectively, in order to maximize the sensitivity to the phase fluctuations of the signal modulation, as discussed in Section 2.4. Following the LO arm the signal propagates through a fibre stretcher[3] meaning the phase of the LO can be stabilized relative to the signal arm. This fibre stretcher is connected to a PID controller[4] which is used to lock the signal to the phase quadrature and stabilize thermal drifts and phase noise of the system, as will be discussed further in Section 3.2.3. The signal then arrives at the final beam splitter where it interferes with the signal arm to generate the homodyne output. The signal arm is sent through the signal modulation, where the signal is modulated by the displacement of the sample. The experimental setup for the signal modulation is shown in Figure 3.3. The modulated signal is thereafter sent through another beam splitter with a coupling ratio of 99:1 in order to measure the intensity of the modulated laser with a photodetector[5]. Finally the signal is sent to the final beam splitter to interfere

---

[1] Toptica Photonics CTL 1500

[2] Thorlabs Fused Fibre Optic Coupler

[3] Optiphase Piezoeletric Fibre Stretcher

[4] Toptica Photonics PID 110

[5] Thorlabs DET01CFC/M

with the LO signal. The two resulting beams, shown in equations (2.22) and (2.23), are then subtracted from one another in a balanced amplified photodetector[6] whose output is a voltage proportional to the intensity difference between the two beams. This electric signal, along with a monitor signal and the signal from the PID, is then sent to an oscilloscope[7] for further analysis. As the frequencies analysed are on the order of 100 Hz to 20 kHz a low-pass filter[8], with a cut-off frequency of 50 kHz, was placed before the oscilloscope for the homodyne output to avoid aliasing issues [41].

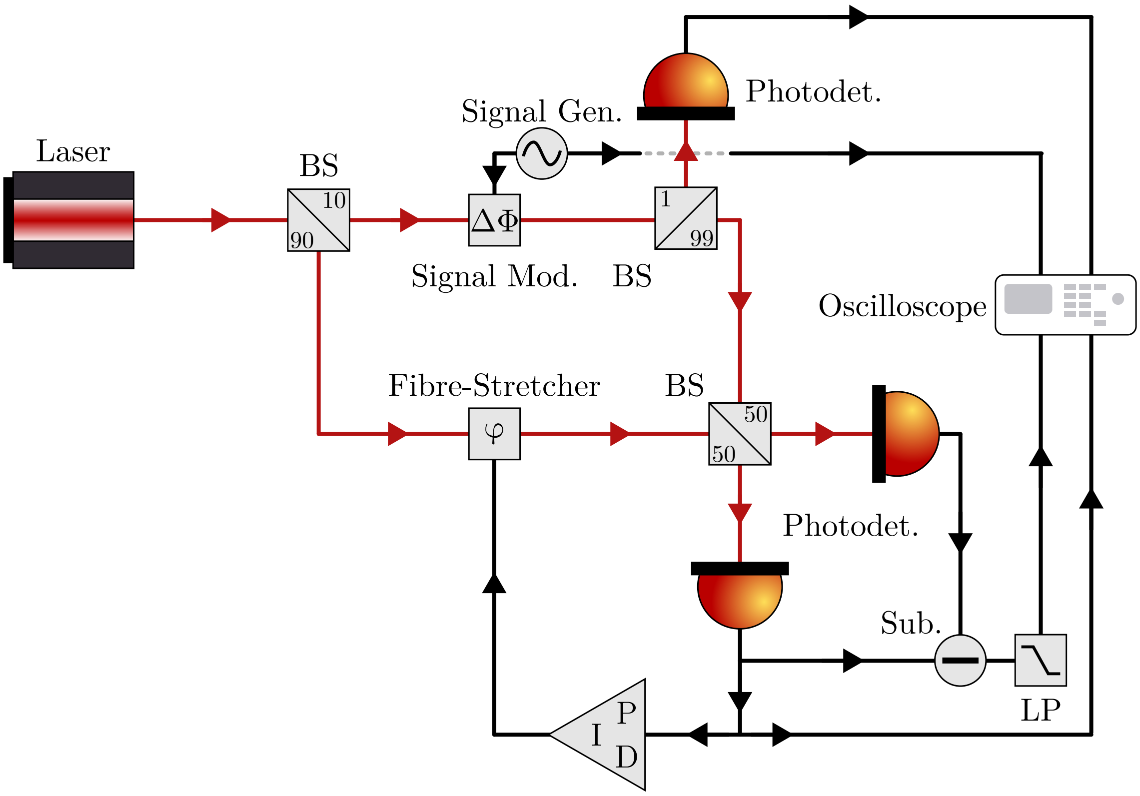

Figure 3.2: Sketch of the experimental setup used for balanced homodyne detection. The system consists of a 1550 nm laser split into two arms by a 90:10 beam splitter. The top arm represents the signal arm where the signal is modulated and its intensity measured with a photodetector. The bottom arm represents the LO arm which acts as a reference. These beams are sent to the 50:50 beam splitter where they interfere and produce an output proportional to the signal modulation. One output of the photodetector is sent to the PID in order to stabilize the relative phase between the signal and LO arms to $\pi/2$ radians to lock to the phase quadrature.

The setup used for modulating the signal arm was based on free-space optics and is shown in Figure 3.3. Here the laser (red) is shown as it propagates from a fibre collimator[9] to the sample and back again via two steering mirrors[10], adjustable in

---

[6] Thorlabs PDB450C

[7] PicoScope 4424a

[8] Thorlabs EF124

[9] Thorlabs F260APC-1550

[10] Thorlabs BB1-E04-10

both yaw and pitch. On the sample a mirror is placed to allow this reflection to occur, with the sample itself being mounted to a transducer[11] which, when driven by a signal generator[12], is able to vibrate at different frequencies. The vibrations will impart a phase shift on the reflected laser, as discussed in Section 2.4, resulting in a shift in the amplitude of the output signal, meaning the modulation can be extracted from it. To perform these measurements the laser needs to be aligned well with regards to the collimator and sample, with a preferred incident angle of 90°. If the incident is not perpendicular to the mirror, then the motion will be offset by an angle. This leads to the laser not registering the real motion of the sample, instead picking up an angular offset. The laser alignment is performed with the help of the two steering mirrors, which allow the required degrees of freedom to align it at the sample and collimator at the same time. First an initial alignment is made, with the laser guided roughly to the centres of both mirrors, with it reflecting back along the same path from the sample. As the laser is non-visible to the eye a laser viewing card[13] was used to observe its path. This leads to a situation where fine-tuned adjustments needs to be made to then line up the laser perfectly. By connecting a power-meter at the laser output, in this case with a photodetector as seen in Figure 3.2, the intensity can be observed as the mirrors are adjusted. Then an adjustment can be made as to turn the mirrors just enough to overshoot a local maxima in intensity. By repeating this many times this process can be used to find the global maximum of the intensity. This maximum is achieved when further repetitions of the above starts to lead to a decreasing intensity, meaning the global maximum has been passed.

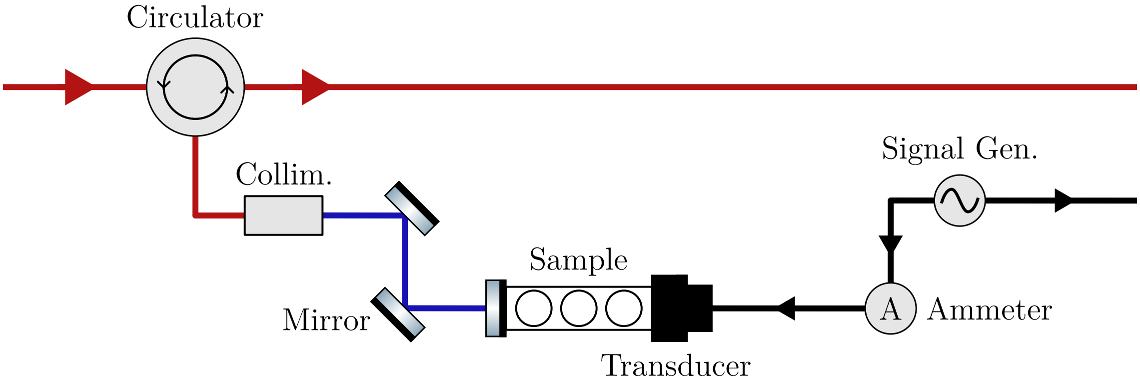

Figure 3.3: Sketch of the free-space setup of the homodyne system. Red indicates a laser travelling through fibre-optic cables, while blue indicates a laser travelling in free space. The task of this system is to impart a phase shift upon the laser dependent on the motion of the transducer. This transducer is sent a signal from a signal generator which passes through an Ampere meter in series to measure the current through it. First the signal is sent through a circulator into a fibre collimator and out into free-space. Here the laser propagates via two steering mirrors onto the sample and is reflected back along the same path. The signal is then sent back the other way through the circulator to the homodyne system.

---

[11] Electrokit Surface Transducer

[12] Keysight 33510B

[13] Thorlabs VRC2

In the ideal case, the coupling between collimator and sample in the free-space setup needs to be as high as possible in order to obtain maximal information and a high-signal to noise ratio. However, in this type of setup the total intensity reflected is not of the greatest importance as long as the signal is above the noise floor of the setup. This is assuming that the beam is still perpendicular to both the sample and collimator, as otherwise the observed motion would be offset by a small angle. If the backreflected power is lowered then the oscillations of the final signal will be lowered as a result. This is compensated for by the calibration of the setup performed, with the voltage to displacement ratio being calculated. However, this will not fix the issue of a non-perpendicular alignment on the sample, with any angular offsets remaining.

3.2.2 Transducer Characterization

A sonic transducer was used to oscillate the mirror in the free-space setup of the homodyne. The transducer used is essentially a loudspeaker with the cone removed, meaning it functions by running a current through a coil which induces a reaction force pushing it up or down depending on the direction of the current. In order to use this as a measurement tool it has to be calibrated first, meaning the electric input to the transducer has to be related to its motion. This can be done by measuring the current I and voltage U through the transducer at a set input voltage from the signal generator over a frequency interval in the sonic range. This creates an electric transfer function of the transducer which can be used to relate the motion of the transducer to the frequency. In Figure 3.4 this frequency response curve is shown for the transducer with an added mass of $m \approx 19$ g where impedance $Z = U/I$ is shown as a function of frequency. A few distinct peaks are visible in the spectrum at around: 425, 4400, and 5900 Hz. These frequencies correspond to the transducer resonances, where the responsivity of the transducer is as high as possible, meaning these frequencies will result in a maximum of motion. This is as opposed to the higher frequencies, where a higher electrical impedance causes the transducer to not move as much. As the transducer is coil-based its impedance can be expressed as $Z = R + iX$, where R is resistance, and $X = \omega L$ is the reactance of the coil. Ignoring losses in the circuit, i.e., $R = 0\ \Omega$, means the magnitude of the impedance becomes $|Z| = \omega L$, i.e. growing linearly with frequency. The acceleration of the transducer has been shown to increase linearly with its input voltage [42], meaning its displacement could be expected to do the same at a specific frequency. The expected vibrational motion can be obtained by assuming a sinusoidal input voltage, $U \propto \sin(\omega t)$, with an impedance $Z \propto \omega$. The force exerted on the magnet in the transducer is given as

$$F \propto I = U/Z \tag{3.1}$$

As $F = ma$ the vibrational motion of the transducer then becomes $u \propto \omega^{-3}$, i.e., decreasing as ω^3 with frequency, as $a = \partial_t^2 u$.

Due to the results presented in Figure 3.4 there are consequences for the possible waveforms that can be used to excite the transducer. Since the response of the transducer is frequency dependent it means that its motion will be as well. Sending

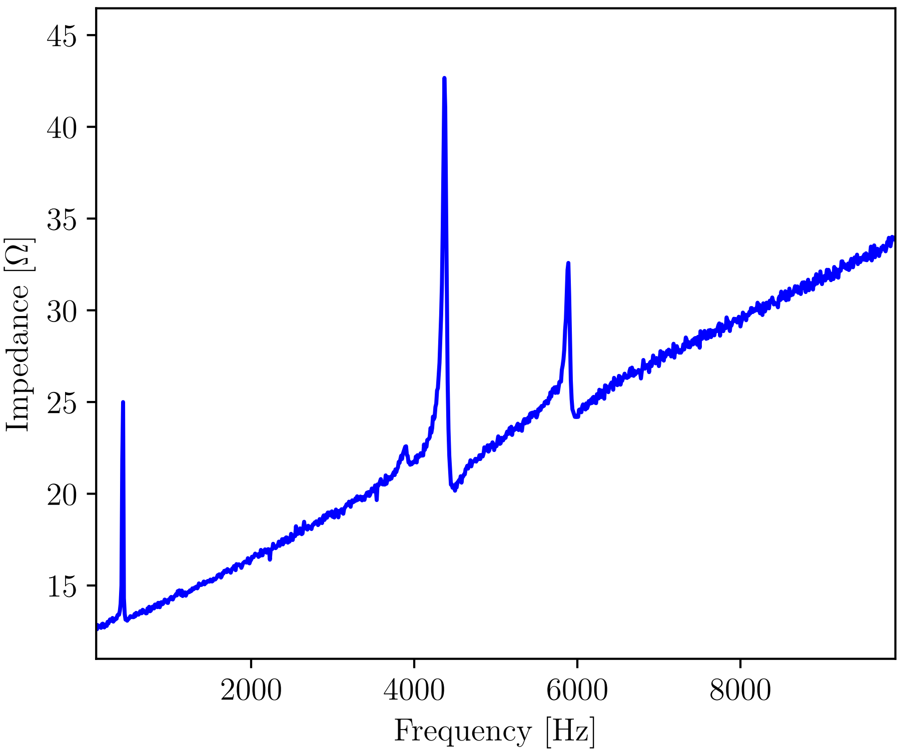

Figure 3.4: Impedance of the transducer as a function of frequencies of 100–15000 Hz. A mostly linear relation between impedance and frequency is shown, with a few distinct peaks visible at frequencies of: 420, 4400, and 5900 Hz, corresponding to resonances.

waveforms that are composed of multiple sinusoidal waves at different frequencies means that different tones will be affected differently, distorting the final signal. For example, a triangle wave is composed of odd harmonics of its base frequency meaning it will become distorted. This means that this setup is limited to using mono-frequency waveforms, i.e. pure sinusoidal waves, even if waveforms with linear parts, e.g. triangle or ramp waves, could be beneficial as well, see Section 3.2.4.

A complication present with resonators in general is their inherent phase shifting around resonances. Due to its resonant nature it will undergo phase shifts in its response resulting in a phase delay between the signal sent to the transducer and the transducer moving. These phase delays are not consistent over all frequencies and will change depending on the resonances the transducer has meaning there will be an inherent phase delay between the input voltage signal and the homodyne signal as well, since the homodyne signal is in phase, disregarding the signal travel time, with the motion. When performing measurements or calibrating the system this phase lag will be ignored as it does not represent any information that is necessary for the purpose of this thesis.

The characteristics of the transducer can also be used as a reference for the homodyne system. In Figure 3.5 an initial displacement spectra (top) is shown at a frequency interval of 1000–15000 Hz for a transducer with an added mirror to reflect the laser, with a weight of about 19 g. The transducer was driven with an input voltage of 1.0 volt at all frequencies. Three distinct peaks can be spotted in this interval: at 3900, 4400, and 5900 Hz, closely following the same pattern as shown in Figure 3.4. The specifics of the calculations behind the displacement is discussed in Section 3.2.4. In a logarithmic scale (bottom) a linear slope can be observed, with a rough estimation for a slope of -2 in log-space, meaning the displacement is proportional to ω^{-2} in linear space. This is not fully consistent with the earlier assumptions made for the transducer, as an ω^{-3}-dependent displacement was theorised, and could likely come as a consequence of the calibration of the setup.

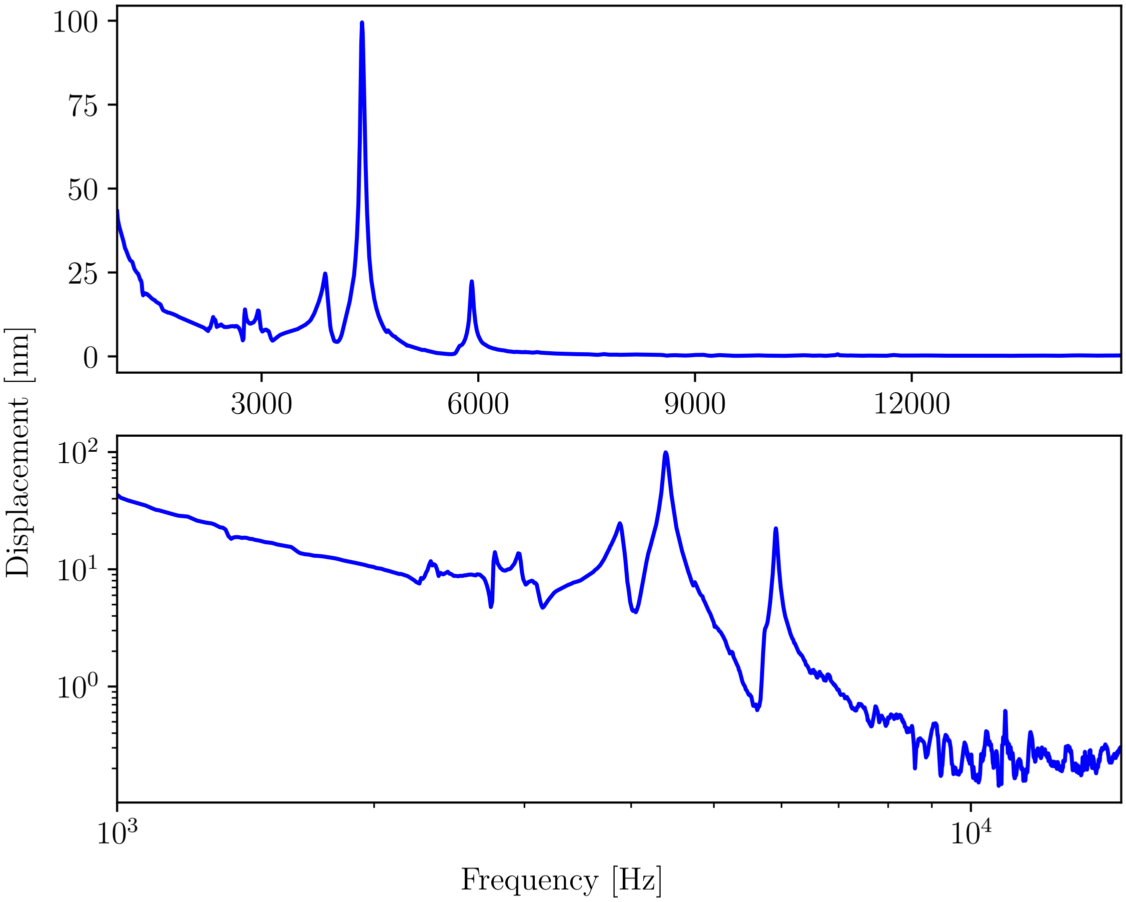

Figure 3.5: Vibrational amplitude in nanometres of the transducer as a function of frequency, both in linear (top) and logarithmic (bottom) scales, driven with an input voltage of 1.0 volt. Peaks can be found at the same frequencies as for its impedance, i.e., peaks corresponding to resonances.

3.2.3 Locking of the Homodyne Setup

In order to measure the phase shifts caused by the vibrations of the transducer the quadrature measured must be the phase quadrature. This means that the relative phase between the LO and signal arm must be $\varphi = \pi/2 + n\pi$, as discussed in Section 2.4. In the ideal case this would simply mean imparting a static phase on either the LO or signal arm for this to work. However, in reality this is not the case. Optical fibres are constantly interacting with the environment meaning they can thermally expand or contract, causing phase shifts which pulls the homodyne away from the desired quadrature. Another factor could be mechanical vibrations in the free-space setup which causes the phase modulation to oscillate. A way to fix this is to use a PID controller [43] to continuously adjust the relative phase using a fibre stretcher. As the thermal drifts are slow, i.e. low frequency, the PID can be used to mitigate them and at the same time avoid affecting the higher frequency signals of interest. Ideally this could be achieved by locking to the intersect point between the monitor outputs of the homodyne, see equations (2.27) and (2.28), leading to the phase $\varphi = \pi/2$. However, the 50:50 beam splitter, see Figure 3.2, does not couple the beams perfectly, instead resulting in a slightly offset split. This can be circumvented by instead locking to the maximum slope of one of these monitor signals, which locks the homodyne to the phase quadrature as well.

3.2.4 Calibration of Displacement

Assuming that the signal obtained with the homodyne detection setup is linear with regards to the motion of the transducer the homodyne output becomes

$$V = \frac{dV}{dx} x, \tag{3.2}$$

where V is the voltage amplitude recorded on the oscilloscope from the homodyne, and x is the displacement. As the homodyne only sees the motion of the transducer, i.e. not what causes it, the derivative in equation (3.2) is constant for the system if all other conditions affecting the readout signal are constant. In theory this means the calibration would only need to be calibrated once, for one frequency, but in reality the calibration is dependent on the whole system, which is often not perfectly independent on frequency. With the product rule the derivative can be further expanded as

$$\frac{dV}{dx} = \frac{dV}{dV_\mathrm{T}} \left(\frac{dx}{dV_\mathrm{T}} \right)^{-1}, \tag{3.3}$$

where V_T is the voltage amplitude of the signal sent to the transducer. The first part of equation (3.3) relates the homodyne voltage to the input voltage to the transducer. This can be determined by plotting the two signals against one another. As stated in Section 3.2.2 the only practical waveform to use is a sinusoidal wave, meaning the output would obtain the same shape if the system was linear. Figure 3.6 shows an experimental demonstration of this, with the output voltage of the homodyne signal shown as a function of the input voltage to the transducer. This results in the ellipse shown, with the eccentricity occurring due to the presence of phase lag between the signals. Disregarding this phase offset, as discussed in Section 3.2.2, the derivative can be calculated as a linear slope

$$\frac{dV}{dV_\mathrm{T}} = \frac{\Delta V_\mathrm{pp}}{\Delta V_\mathrm{Tpp}}, \tag{3.4}$$

where ΔV_{Tpp} and ΔV_{pp} are the peak-to-peak voltages of the output and input voltage signals respectively. These measurements are made under the assumption that the output is linear with regards to the motion.

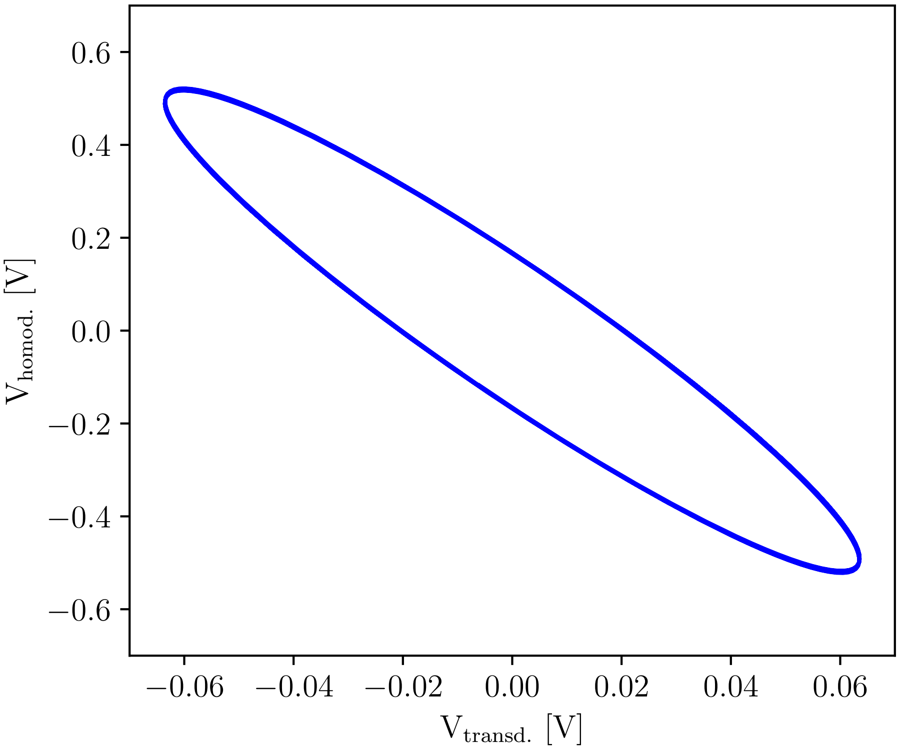

Figure 3.6: Example of a linear calibration measurement where the output voltage of the homodyne is plotted against the input voltage to the transducer. The resulting shape is an ellipse from which the amplitude ratio between the signals can be extracted.

The second part of equation (3.3) corresponds to the relation between the change in motion of the transducer because of its input voltage. This factor can be calculated by obtaining a reference, where a known distance is measured as a result of a known input voltage. As the laser wavelength is known it can be used for this purpose. As the transducer moves exactly $\lambda/2$ the output will be phase shifted by exactly one period, as $kx = 2\pi$ as the laser is reflected. So, for example, if the transducer moves by a distance of 2λ four full oscillations will have happened. Thus, by counting the number of oscillations, N, the total distance the mirror has moved is known. In Figure 3.7 the homodyne and transducer signals are shown as a function of time. Here the linear region of the sinusoidal is shown with the oscillations that has arisen as a consequence of the distance travelled. This can be calculated as

$$\frac{dx}{dV_{\mathrm{T}}} = \frac{\Delta x}{\Delta V_{\mathrm{T}}} = \frac{N \cdot \lambda/2}{\Delta V_{\mathrm{T}}}, \tag{3.5}$$

where ΔV_{T} is a linear change in the input voltage to the transducer. These measurements require the transducer to move a distance of at least $\lambda/2$ in order to see these effects, meaning the output will be non-linear with regards to the voltage input. Thus these non-linear motions are preferably measured around the mechanical resonances of the transducer as its amplitude of motion is at its highest. Finally, by inserting equations (3.4) and (3.5) the total calibration constant in equation (3.3) becomes

$$\frac{dV}{dx} = \frac{2\Delta V_{\mathrm{pp}}\Delta V_{\mathrm{T}}}{\Delta V_{\mathrm{Tpp}} \cdot N\lambda}. \tag{3.6}$$

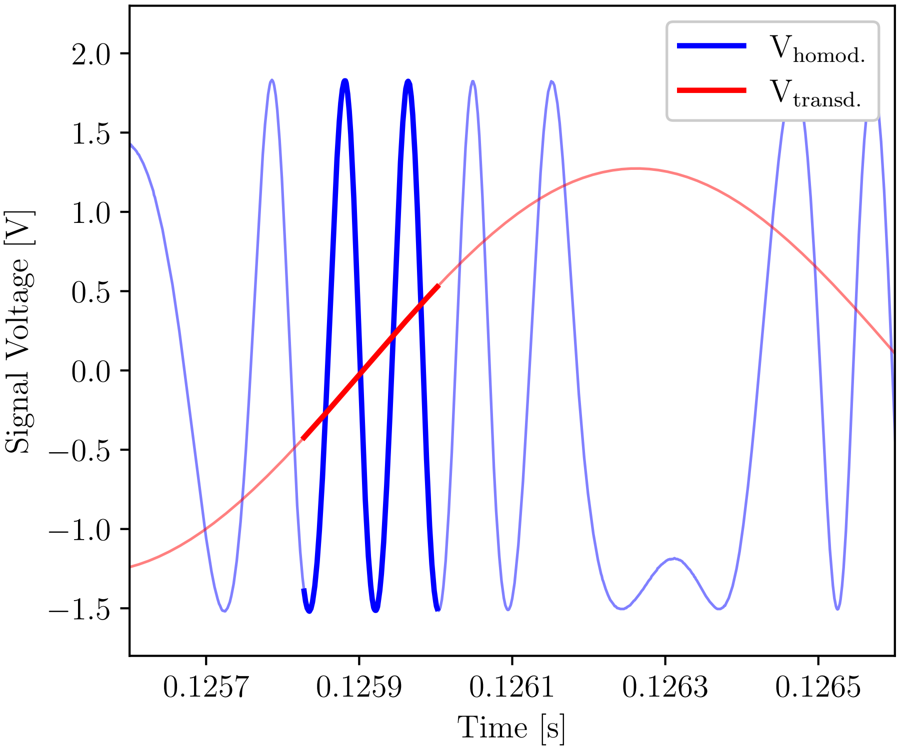

Figure 3.7: Example of a non-linear calibration measurement with the output voltage of the homodyne (blue) and input voltage to the transducer (red) shown in time. A linear slope of the transducer voltage is highlighted where the number of oscillations can be counted to determine the total distance travelled.

4
Results

In this chapter the results and discussions of the thesis are presented, including the design and simulation of samples, the characterization of the experimental setup, and the results of the displacement measurements of fabricated acoustic metamaterials.

4.1 Samples

In Figure 4.1 the design of the fabricated sample is shown, with a single unit cell (left) and the complete sample (right). The unit cell consists of an outer matrix and an inner core connected by thin arms, placed at an angle $\Theta = 45°$ from the vertical axis. The lattice constant of the cells $a = 3$ cm, with inner and outer diameters $d = 2.1$ cm and $b = 2.7$ cm, respectively. The connections between the core and matrix were made in two configurations, with $c_1 = 0.5$ mm and $c_2 = 1.5$ mm. This design was inspired by the work of Jiang et al. [44] who, with a similar design in three dimensions, achieved a complete band gap at frequencies lower than the corresponding Bragg scattering band gap of the same design. The design presented in this thesis is different in a few ways: it was created in two dimensions, and the core is smaller relative the unit cell as a result of this. As discussed in Section 3.1, the choice of two dimensions was made due to fabrication, as the two dimensional design could be completed with laser cutting only. These samples were made with an acrylic plastic, see Table 4.1, which meant the sample thickness became 5 mm, as that was the sheet thickness of the acrylic. A thicker sample would have been preferable due to the structural stability of the sample, as the thin plastic resulted in the sample bending slightly, as it does not significantly impact the dispersive qualities of the unit cell along the x-axis.

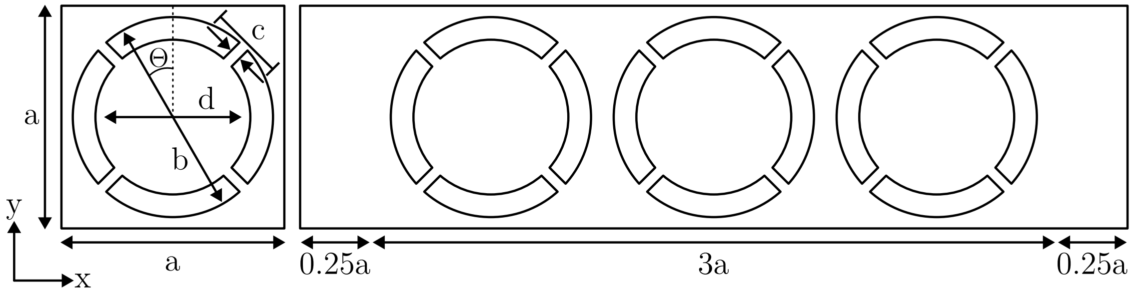

Figure 4.1: Design of fabricated samples with the unit cell (left) and the complete sample (right). Padding on either side in the complete sample to mount screws.

The complete sample, shown in Figure 4.1, consisted of three unit cells in series, with buffer zones at the edges, with width $a/4$, added to allow for fastening the sample with screws and mount a mirror to it. The choice of three unit cells was made to keep the sample as small as possible, while still allowing for a reasonable level of attenuation to occur, which will be discussed in Section 4.2. A simple bulk sample was also fabricated along with the metamaterial samples for comparing the displacement of the different samples. The c_1-metamaterial had the added caveat of structural supports being necessary at the connections due to them being too thin for the laser cutting. Figure 4.2 shows the finalised fabricated samples, with the bulk sample (left), and metamaterial samples corresponding to the c_1 (centre) and c_2 (right), respectively.

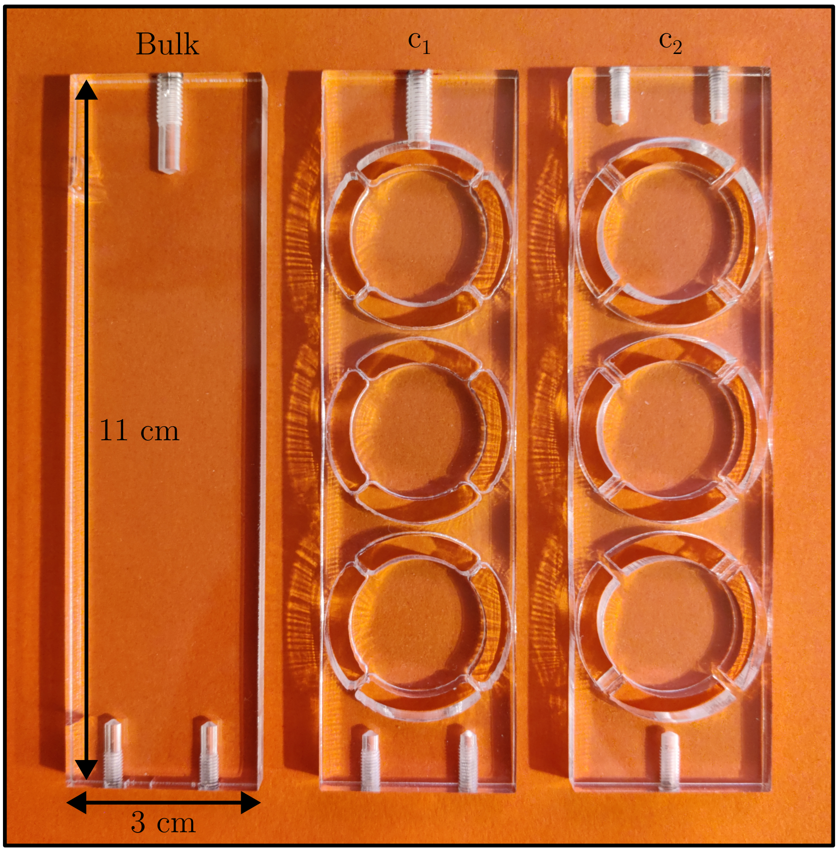

Figure 4.2: Fabricated samples, with the bulk sample (left), and metamaterial samples corresponding to c_1 (centre) and c_2 (right). Here small deformations due to fabrication can be seen with uneven walls and connections in the samples.

Other samples presented were only simulated, with the initial design shown in Figure 4.1 being modified with different material choices, and its internal geometry optimized. Figure 4.3 shows the division of the simple unit cell, with three different sections noted: the outer matrix, the inner core, and the connections between them. The materials of these sections was changed to study the effect of different elastic moduli and densities on the performance of the metamaterial. The materials used are listed in Table 4.1.

Table 4.1: Relevant material properties for acrylic, nylon, Teflon [45, 46], copper, iron, lead [6], and tungsten, all at room temperature [40]. Also shown is the speed of sound in the longitudinal direction, as calculated with equation (2.15).

Material	Density [$\mathrm{kg\,m^{-3}}$]	Young's Mod. [GPa]	Poisson's Ratio	c_ℓ [$\mathrm{ms^{-1}}$]
Acrylic	$1.19 \cdot 10^3$	3.2	0.35	$2.08 \cdot 10^3$
Nylon	$1.15 \cdot 10^3$	2.0	0.40	$1.93 \cdot 10^3$
Teflon	$2.17 \cdot 10^3$	0.5	0.47	$1.18 \cdot 10^3$
Copper	$8.96 \cdot 10^3$	110	0.35	$4.44 \cdot 10^3$
Tungsten	$17.8 \cdot 10^3$	360	0.28	$5.08 \cdot 10^3$
Iron	$7.87 \cdot 10^3$	200	0.29	$5.77 \cdot 10^3$
Lead	$11.3 \cdot 10^3$	40.1	0.37	$1.15 \cdot 10^3$

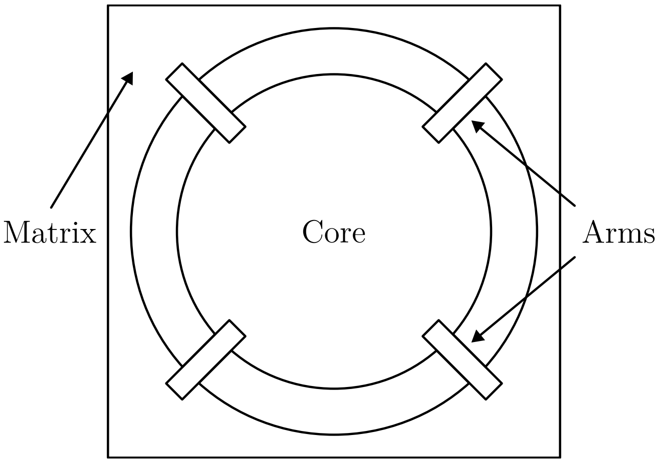

Figure 4.3: Partition of the unit cell into zones that were changed to different materials during simulations of the metamaterials.

4.2 Metamaterial Simulation

This section presents the simulations performed for the samples. Here both the dispersion relation and transmission spectra for each respective sample is shown and discussed.

4.2.1 Fabricated Samples

Figure 4.4 shows the dispersion relation for the two variations in the first sample, with $c_1 = 0.5$ mm and $c_2 = 1.5$ mm shown from left to right. This relation shows the solutions to ten eigenfrequencies, corresponding to ten modes of vibration in the sample. In both dispersion relations, multiple band gaps can be spotted, with a complete band gap (CBG) at higher frequencies and a directional band gap (DBG) at lower frequencies. For c_1, these band gaps are located at approximately 19.0–24.1 kHz and 6.9–8.4 kHz, respectively, while for c_2 they are located at 21.6–24.2 kHz and 10.6–12.2 kHz. The complete band gaps shown in either case are likely caused by Bragg scattering as the frequency interval is mostly unaffected by local changes in the unit cell. For acrylic, with unit cell sizes of 3 cm, the expected frequency of a Bragg scattering band gap occurs at roughly 35 kHz, see Table 4.1 for material properties, aligning well with the observed complete band gap. The directional band gaps located at lower frequencies are present as the wave propagates from Γ to X, meaning wave propagation corresponding to those wave vectors is forbidden. Thus waves propagating purely in the x-direction are likely to be attenuated. However, since the band gap is not complete, i.e. only directional, phonons corresponding to modes in Γ to M or X to M may still propagate at this frequency interval.

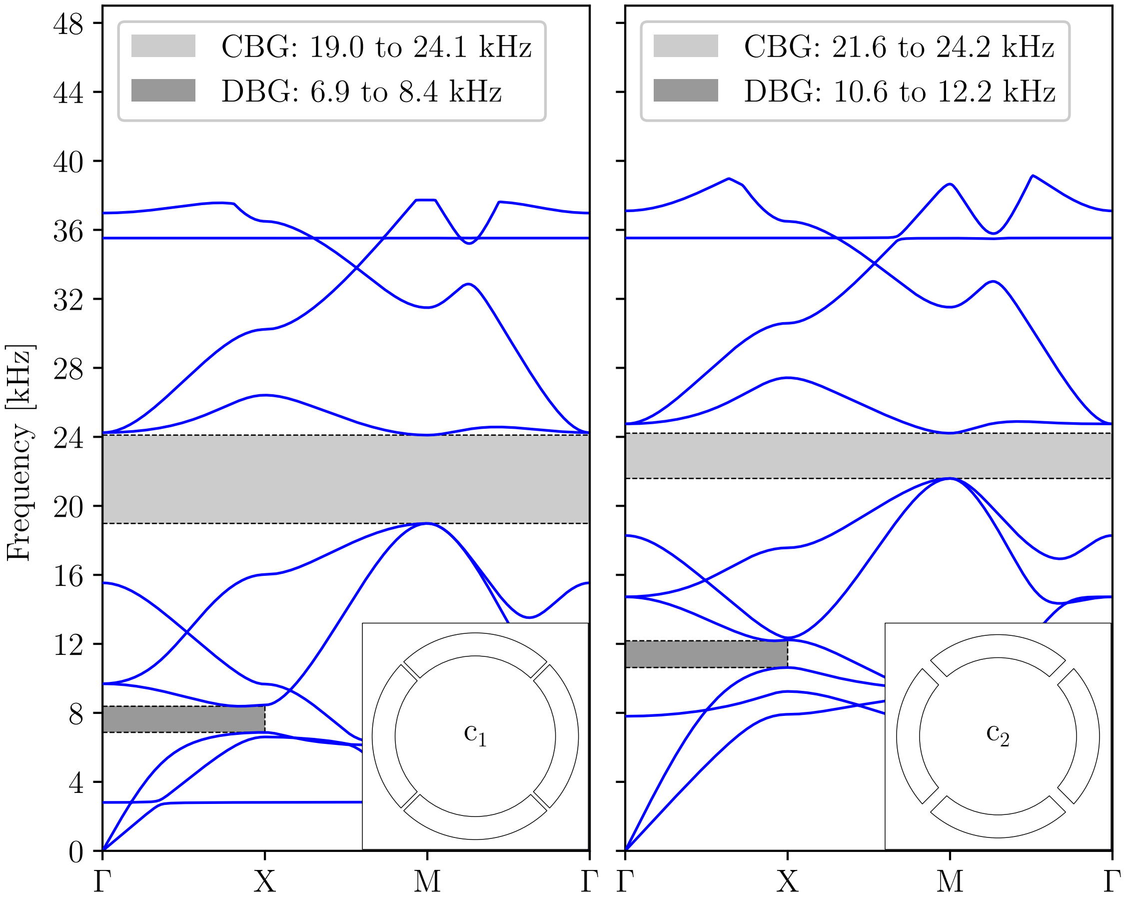

Figure 4.4: Dispersion relations for c_1- and c_2-metamaterials, shown from left to right. Complete band gaps are visible at frequencies of about 19.0–24.1 kHz, and 6.9-8.4 kHz, with directional band gaps, between Γ and X, at 21.6–24.2 kHz, and 10.6–12.2 kHz for c_1 and c_2, respectively.

Figure 4.5 shows the transmission spectra (top), with c_1 and c_2 shown in red and blue, respectively. Here two distinct dips in transmission can be found in both spectra, at roughly 6–13 kHz and 10–14 kHz for c_1 and c_2 with attenuation levels of about 45 and 70 dB, respectively, corresponding to frequencies of the directional gaps in Figure 4.4, whose predicted band gaps are shown as shaded regions. This attenuation is evidently not infinite, as expected with a finite-size metamaterial. However, with the finite sample simulated, see Figure 4.1, this is not a full representation of the band structure. At higher frequencies another dip in transmission can be observed, for both samples, corresponding to the complete band gaps in the dispersion relation. These transmission dips are mostly in agreement with the dis-

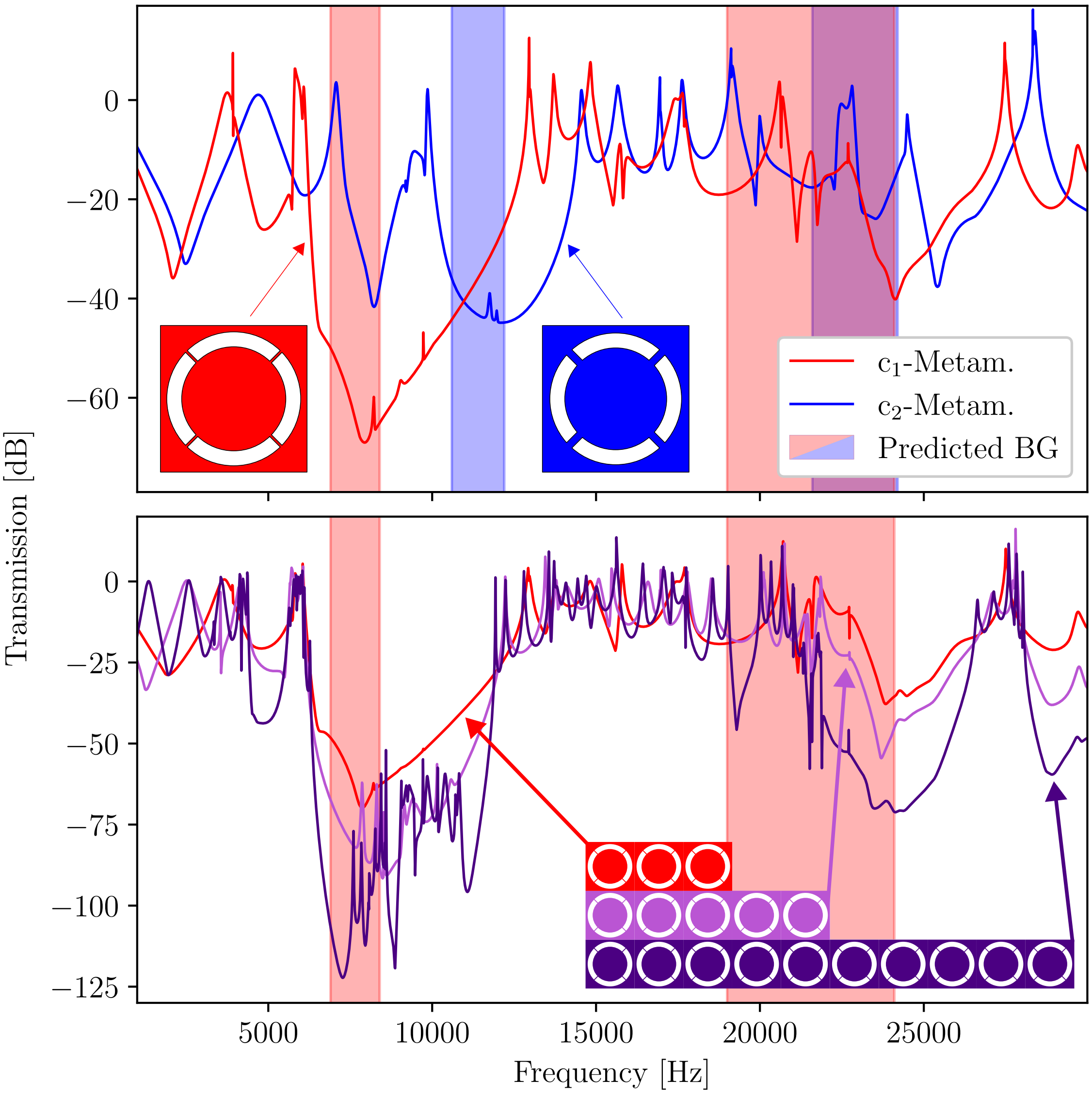

Figure 4.5: Transmission spectra for c_1- and c_2-metamaterials, shown in red and blue, respectively, with three unit cells in series (top). Band gaps predicted with the simulations of the dispersion relations are shows as shaded regions for the respective metamaterial samples. (Bottom) Transmission spectra for c_1-metamaterial with the number of unit cells in series going from 3 (red) to 5 (purple) to 10 (indigo).

persion relation, with differences caused by the finite representation. If the number of cells is instead varied (bottom) the resulting transmission dips become deeper, with minor improvements in frequency accuracy compared to the dispersion relation. Here the number of cells is chosen as 3 (red), 5 (purple), and 10 (indigo). At the low frequency band gap, in particular, the transmission has decreased by a significant amount when increasing the number of cells from 3 to 10. Other dips present in the spectra, such as the one located around 8 kHz for the c_2-metamaterial, can not be fully explained by the dispersion relation of the unit cell. These dips are instead likely caused by the finite nature of the complete sample, with edge-effects or reflections not accounted for in the dispersion relation causing artefacts to appear. In particular, at higher frequencies inconsistencies in these simulations could be caused by the meshing of the model in COMSOL. The size of the meshing is decided by the frequencies studied, as meshing elements that are larger than the studied wavelength results in a worse representation of the physics, as the discretized elements are no longer regarded as single effective materials by the incoming wave.

As seen in Figures 4.4 and 4.5 the band gaps and transmission dips are dependent on the internal geometry of the unit cells. For example, comparing the dispersion relations of the c_1- and c_2-metamaterials it can be observed that by simply changing the width of the connections inside the unit cell the band structure changes significantly. This means that the dispersion relation can be optimized. In Figure 4.6 the correlation between the directional band gap frequency interval and the connection width c is shown. Here the upper and lower bands of the transmission dip are marked in red and blue, respectively, with the frequency interval between them corresponding to the band gap. This results in a clear correlation where lower values of c leads to a reduction in the lower frequency band, meaning the band gap occurs at lower frequencies, while the upper band follows a similar trend. As the connections

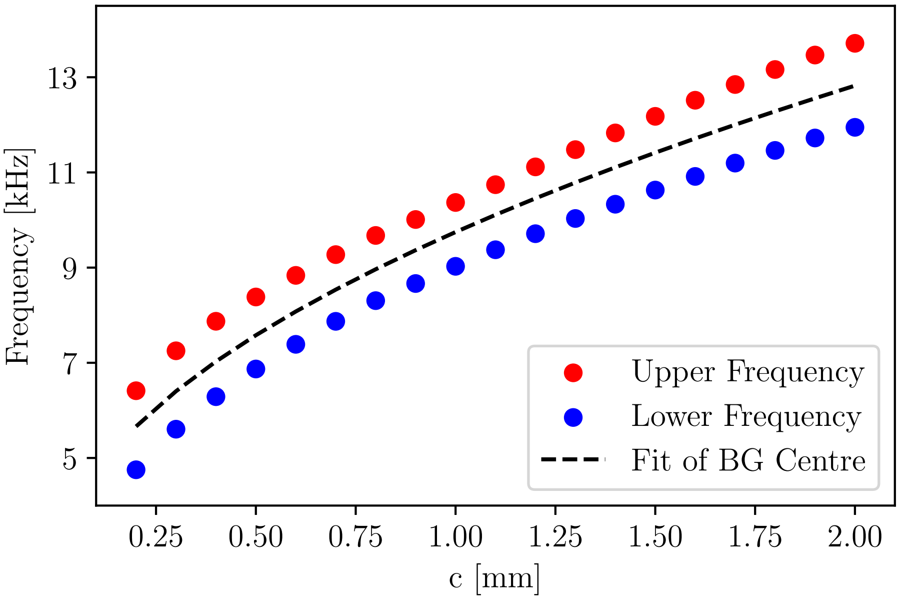

Figure 4.6: Optimization plot for width c of the connections where frequencies of the upper (red) and lower (blue) bands of a directional band gap are plotted as a function of c. Fit of central frequency of the band gap (black) shown with frequency proportional to $c^{0.505}$, with a clear decrease in the band gap location observed as c gets smaller.

get thinner the coupling between the matrix and core is getting smaller, as a thin structure will be more prone to deformation and bending, meaning the core will be able to move more freely. Comparing this with a simple mass-spring system where $\omega = \sqrt{k/m}$, if the spring constant gets smaller, so does the resonant frequency. By treating the coupling of the connections to the core as a spring this decrease in coupling should also decrease the resonant frequency of the resonator. Meaning the band gap appears at a lower frequency. Fitting the central frequency points between the bands to a function of the form $f(c) = \alpha c^{\beta} + \gamma$ leads to: $\alpha = 7345.8 \pm 204.0$, $\beta = 0.505 \pm 0.015$, and $\gamma = 2401.4 \pm 194.8$, with $\mathrm{R}^2 = 0.9997$ (coefficient of determination). Thus the band gap central frequency is approximately proportional to the square root of the connection width c, replicating that of a harmonic oscillator.

Another factor that may be changed is the diameter d of the inner core. Figure 4.7 shows the upper and lower frequencies of the directional band gap as a function of the ratio between the inner diameter and lattice constant d/a, where the upper and lower frequencies are shown in red and blue, respectively. These simulations were performed with $c = c_2$ and $b = 2.7$ cm. As the ratio increases from 0.60 to 0.875 a minimum value in the band gap frequency can be observed at around 0.65 to 0.70. However, the frequency interval continues to increase while the ratio grows. As the diameter of the core grows, so does its mass. Again, assuming a simple model of a resonator, with $\omega = \sqrt{k/m}$, this is expected. Thus, in theory, the larger the diameter the lower the bandgap. In reality this is not the case, when the diameter grows the soft connections between matrix and core get smaller, meaning there is both less room to oscillate and a stiffer connection to the matrix. This means that there is some optimum value in between these two, which is found in this optimization.

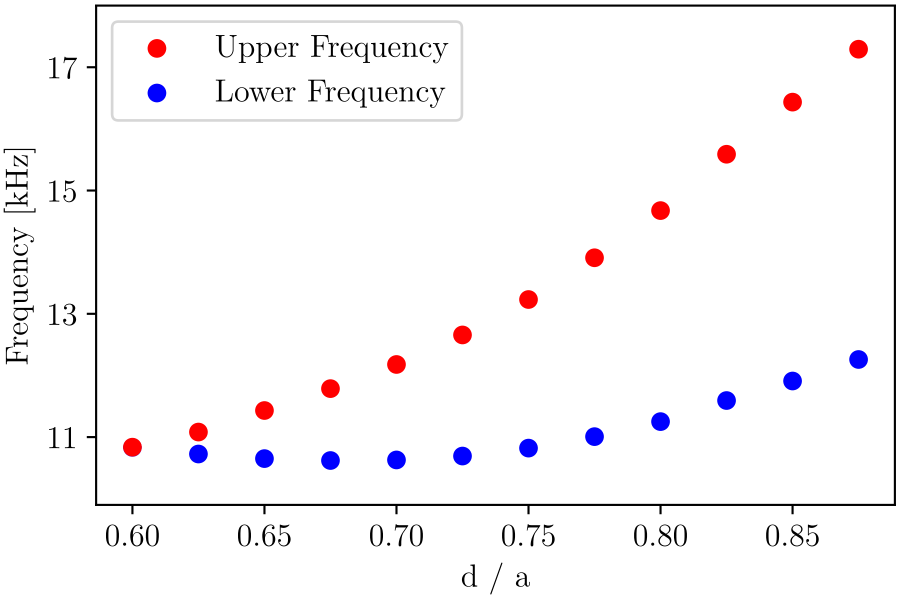

Figure 4.7: Optimization plot for the inner diameter d where the frequency of the upper and lower bands of a directional band gap are plotted as a function of d/a, where a is the unit cell width and $c = c_2$. A minimum is located at $d/a = 0.675$.

At frequencies and bands corresponding to band gaps, or dips in transmission, it is of interest to observe the different modes of vibration present. Figure 4.8 shows a few vibrational modes present as the dispersion relation is simulated. In Figures 4.8a and 4.8b two modes at the upper and lower bands of the DBG, respectively, are shown at the X-point, i.e., $\mathbf{k} = (\pi/a, 0)$. Maximum displacement is visualised in a dark blue, with green meaning low to no displacement in the mode. These modes show the core oscillating either in opposition to the rest of the cell, or at least independently from it. This is typical behaviour of a local resonance, where the core becomes decoupled from the rest of the structure. At the lower band the core is oscillating freely against the matrix, while at the upper band the core is staying still with the matrix moving against it. In contrast, in Figure 4.8c a point at the first acoustic band is shown, specifically at $\mathbf{k} = (\pi/2a, 0)$, where the whole cell is shown oscillating in-phase.

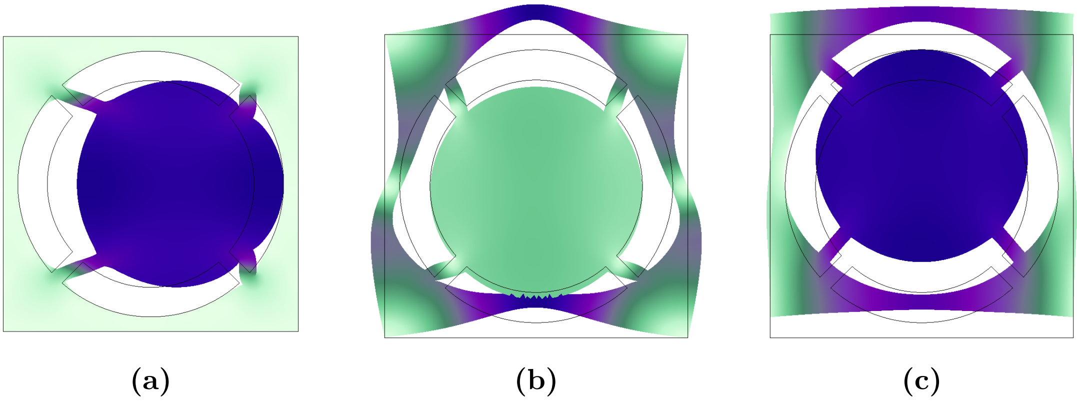
(a) (b) (c)

Figure 4.8: Vibrational modes of the unit cell for the c_2-metamaterial, with dark blue indicating a larger motion and green indicating little to zero motion. These modes are taken from three different points in the dispersion relation, with (a) and (b) corresponding to the upper and lower bands of the directional band gap, respectively, at X. In (c) a mode at halfway between Γ and X is shown for the first acoustic band.

4.2.2 Composite Material Samples

Other samples were simulated to study the effects of introducing material contrasts on its dispersive qualities. All following simulations were performed with structure parameters of $c = 0.5$ mm and $d = 2.1$ cm. Figure 4.9 shows the dispersion relation corresponding to the core of the sample being switched from acrylic to tungsten, a material which is both much heavier and less elastic, see Table 4.1. This results in complete band gaps being observed at frequencies of 2.0–3.7 kHz as well as 19.2–24.1 kHz. The higher frequency band gap is again shown to be mostly independent of the properties within the sample, with the heavier and stiffer core not significantly affecting the location of said band gap, see Figure 4.4. However, the complete band gap at low frequencies is affected by it. As discussed in relation to the optimization of the core diameter d, the mass of the oscillating core is expected to be a significant factor in determining the frequency at which this local resonance occurs. Tungsten is over ten times heavier than acrylic and thus the frequency of the band gap is expected to decrease with it. By then changing the tungsten to another material, iron, similar effects can again be observed with the lower band of the band gap rising from 2.0 to 2.3 kHz, while the upper band remains unchanged. This shows that the behaviour of the band gaps at low frequencies is directly tied to the properties of the core material with higher frequencies remaining mostly unaffected by it.

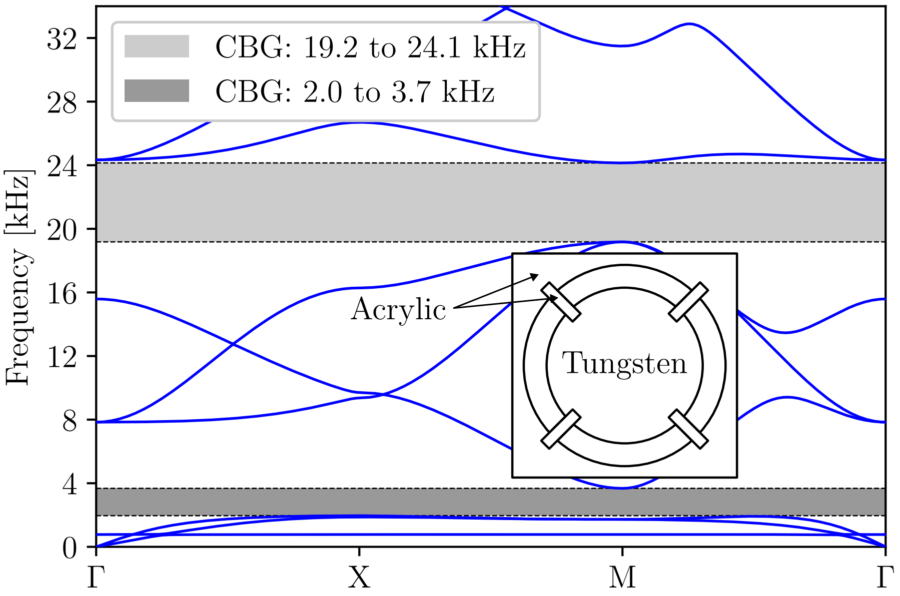

Figure 4.9: Dispersion relation with core switched from acrylic to tungsten. Observable complete band gaps at roughly 2.0–3.7 kHz, and 19.2–24.1 kHz.

As acrylic is not a material that is suitable for use at cryogenic temperatures, as it becomes too brittle and stiff, the remaining polymer is switched out to copper. I.e., changing the material of the connections and matrix while keeping the tungsten core. Copper, in particular, was chosen as it is a common material inside cryogenic environments, as well as its thermal conductivity being significantly better than acrylic, meaning this sort of material composition represents a more realistic scenario. This results in the dispersion relation shown in Figure 4.10 where the complete band gap at low frequencies has disappeared, with a directional band gap instead appearing at frequencies of 11.0–17.9 kHz. As copper is a much stiffer material than acrylic this is probably the reason that the band gap shifts so significantly, with the arms in particular being important for the location of the band gap, see Figure 4.6. This change in material also results in a significant change in the location of the upper complete band gap, with the expected Bragg scattering band gap frequency of approximately 74 kHz for a pure copper phononic crystal, see Table 4.1.

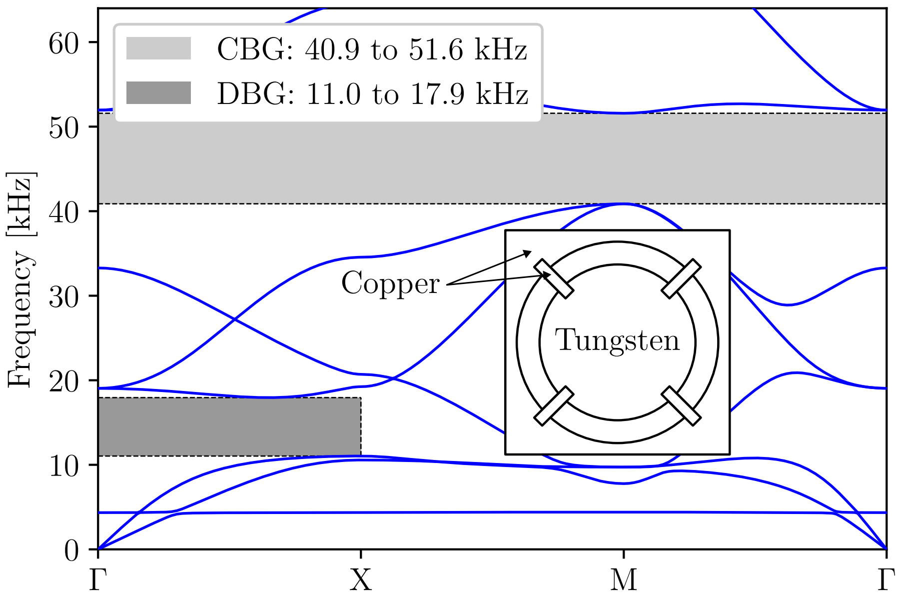

Figure 4.10: Dispersion relation with matrix and arms switched from acrylic to copper, with the tungsten core remaining. Observable complete band gap at roughly 40.9–51.6 kHz, with a directional band gap found at 11.0–17.9 kHz.

The desired function of the metamaterial core is to oscillate independently of the rest of the sample. By making the connections between the matrix and core more flexible the coupling between them is lowered, allowing the core to move more freely. However, this connection cannot be made too flexible as it still needs to hold its place to function as required. One material with a low elasticity modulus is nylon, see Table 4.1. At cryogenic temperatures its elastic moduli will increase meaning it becomes more brittle but will still possess a flexibility that exceeds most metals [26]. Figure 4.11 shows the dispersion relation as the arms are changed from copper to nylon, with the copper-matrix remaining. This results in a low frequency complete band gap at 1.8–3.1 kHz, indicating that making these connections as soft as possible is of significant interest when creating a metamaterial of this nature.

Switching out the nylon for a metal more suitable for cryogenic applications could make this composite structure more practical. One such metal could be lead as it is very flexible compared to other pure metals, see Table 4.1. Figure 4.12 shows the dispersion relation as this change is made. This results in a directional band gap at frequencies of 7.4–12.8 kHz, which is an interval comparable to the sample made purely from acrylic, a highly elastic material. This sample has the added advantage of the copper matrix, raising thermal conductivity and allowing for more effective thermalization in a low temperature environment.

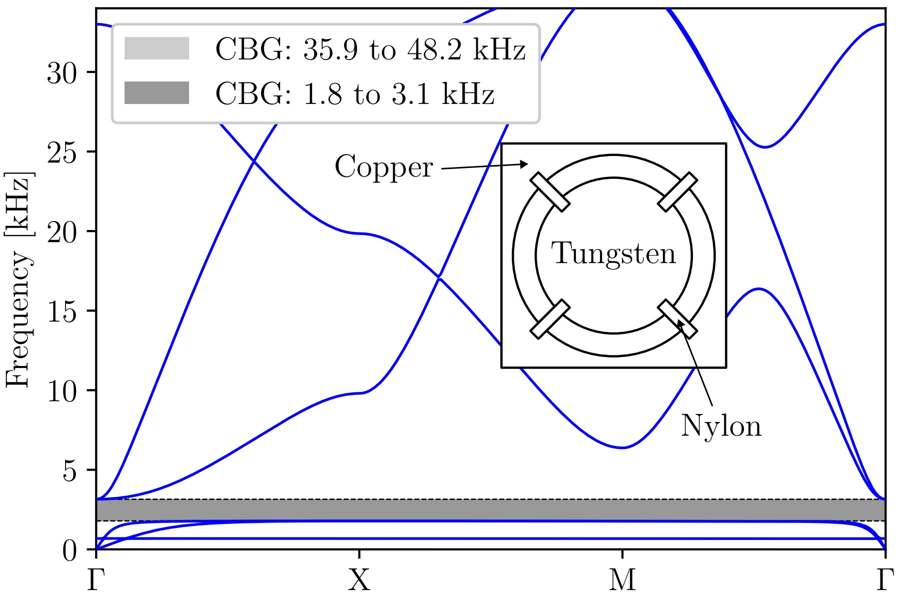

Figure 4.11: Dispersion relation with arms switched from copper to nylon, with the tungsten core and copper matrix remaining. Observable complete band gap at roughly 1.8–3.1 kHz, with the higher frequency band gap remaining at roughly the same frequencies as with the copper arms.

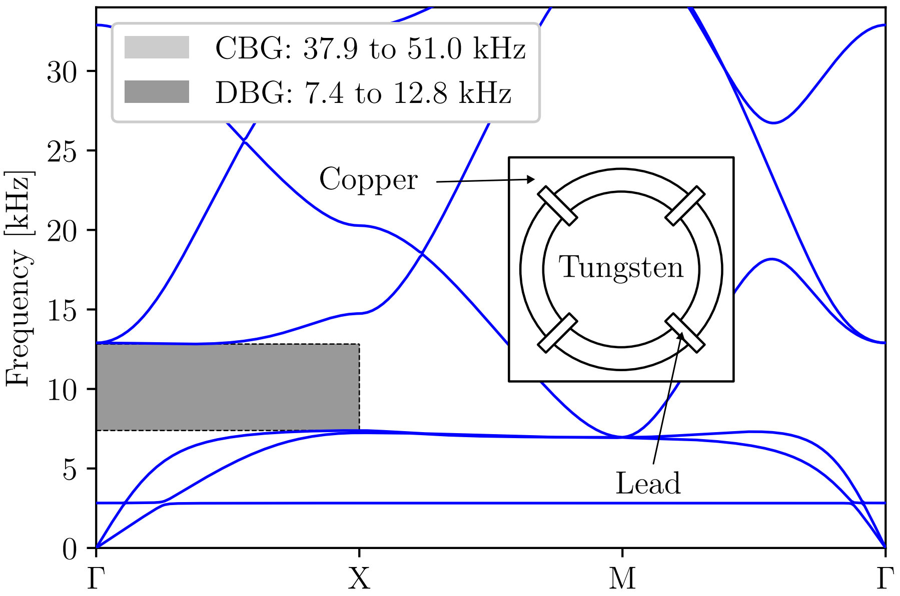

Figure 4.12: Dispersion relation with arms switched from nylon to lead, with the tungsten core and copper matrix remaining. Observable directional band gap at roughly 7.4–12.8 kHz, with the higher frequency band gap remaining at roughly the same frequencies as with the copper and nylon arms.

Finally, a sample consisting of a matrix of Teflon, connections of nylon, and a core of copper was simulated. This resulted in the dispersion relation shown in Figure 4.13 where a directional band gap has formed at 1.9–3.2 kHz, with a complete band cap at 7.2–7.5 kHz. With Teflon being a soft material, see Table 4.1, and replacing the copper matrix with it this behaviour could be expected, as already seen in Figure 4.10 where a stiffer matrix material leads to a higher band gap. By softening the matrix the unit cell's static stiffness is lowered, leading us to a similar situation where the connections were softened. The complete band gap is observed at rather low frequencies, with the likely explanation coming from the reduction in the speed of sound in Teflon compared to both copper and acrylic, leading to Bragg scattering occurring at lower frequencies. However, even though low frequency band gaps were created with Teflon as a matrix material a consequence becomes the thermal conductivity. As Teflon is a thermal insulator, the thermalization of the sample will become much worse than when using a good thermal conductor, like copper.

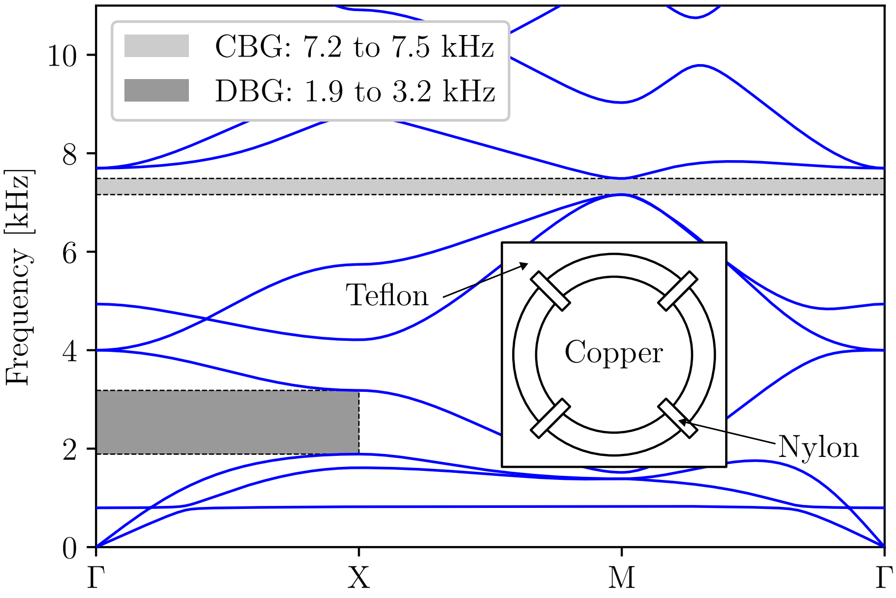

Figure 4.13: Dispersion relation with matrix and core switched from copper to Teflon, and tungsten to copper, respectively, with the nylon arms remaining. Observable complete band gap at roughly 7.2–7.5 kHz, with a directional band gap found at 1.9–3.2 kHz.

In Table 4.2 a summary of the simulation results concerning composite materials is shown, with corresponding final conclusions of each respective simulation summarised and the lowest frequency band gap presented, with superscripts ^{C} and ^{D} corresponding to a complete and directional band gap, respectively. In total, seven different material combinations were simulated, with a general consensus of lower stiffness leading to a lower frequency band gap. In particular, a looser connection between the core and matrix results in a much lower band gap compared to a stiff connection. A softer matrix material also results in this reduction, with the softer Teflon and acrylic, see Table 4.1, shifting the frequency of the band gap down.

Table 4.2: Summary of results of the metamaterial simulations, with material composition and final conclusions of each respective simulation. Band gaps (BG) correspond to the lowest found band gap, with superscripts C and D corresponding to a complete or directional band gap, respectively.

#	Matrix	Core	Arms	BG [kHz]	Conclusion
1	Acrylic	Acrylic	Acrylic	$6.9–8.4^{\mathrm{D}}$	Adequate metamaterial at room temperature, serves as a baseline for the following simulations.
2	Acrylic	Acrylic	Tungsten	$2.0–3.7^{\mathrm{C}}$	Significant reduction in band gap frequency due to higher mass of core compared to acrylic.
3	Acrylic	Acrylic	Iron	$2.9–3.7^{\mathrm{C}}$	Similar characteristics of tungsten core, with slightly higher band gap frequency.
4	Copper	Copper	Tungsten	$11.0–17.9^{\mathrm{D}}$	Stiffer arms leads to an increase band gap frequency, not offset by the high mass core. Copper matrix means better thermalization compared to acrylic.
5	Copper	Nylon	Tungsten	$1.8–3.1^{\mathrm{C}}$	More flexible arms leads to reduction in band gap frequency. Coupled with added thermalization of copper.
6	Copper	Lead	Tungsten	$7.4–12.8^{\mathrm{D}}$	Higher stiffness of lead, compared to nylon, leads to an increase in band gap frequency. However, stiffness of lead more temperature independent than polymers.
7	Teflon	Nylon	Copper	$1.9–3.2^{\mathrm{D}}$	A more flexible matrix material, Teflon, leads to reduction in the frequency of the band gap. However, with worse thermalization, as Teflon is a thermal insulator.

4.3 Experimental Characterization

In this section the experimental measurements and results are presented, with characterization and calibration of the optical setup followed by displacement measurements of the studied samples, with comparisons between bulk and metamaterial samples performed to determine the attenuation caused by the metamaterial. In this thesis measurements were made on three different fabricated samples, along with a reference measurement with the transducer, only loaded with a mirror to enable the optical interferometry. The samples can be seen in Figure 4.1. Table 4.3 shows the weight of each sample setup as that impacts the mechanical resonances of the transducer.

Table 4.3: Weight of each studied sample, with different weights loaded onto the transducer leading to the shift in resonance frequencies, and corresponding amplitudes.

Sample	Mirror	Bulk	c_1-Metamaterial	c_2-Metamaterial
Weight [g]	19	48	43	38

The background noise present during the experiments can be characterized by the power spectral density (PSD) of the setup without any added vibrations from the transducer. This PSD is presented in Figure 4.14 where the spectral power, in units of V^2/Hz, is plotted against frequency at two scenarios: with the signal generator being switched off, and with it on with a tone of 6000 Hz and peak-to-peak voltage of one volt. This frequency was chosen as it occurs at a frequency where background noise is flat. The background and tone are shown in blue and red, respectively, and each consist of five different measurements, overlaid on top of each other to observe the consistency of the noise. At low frequencies the noise is largest, with high noise at frequencies below 6000 Hz in particular. This noise most likely corresponds to noise from the environment with, for example, mechanical vibrations affecting the free-space setup. At higher frequencies this noise dies down and becomes much smaller. At 6000 Hz the input tone is clearly visible, with its peak-value being five orders of magnitude larger than the noise at the same frequency. As this peak is singular, and does not come with any strong harmonics the homodyne response to the motion is assumed linear in this case. Although, this is not strictly enough to determine this. This has to be done by observing how much the output signal rises when the input voltage to the transducer increases. If this increase is linear, i.e., if the input voltage doubles then the output voltage also doubles, then the signal can be safely regarded as linear. The signal to noise ratio SNR $\approx$ 42 dB at this frequency, calculated by dividing the integrated signal with the integrated noise around the peak at 6000 Hz. However, as the motion of the transducer is dependent on the frequency the SNR will be as well, meaning different input voltages are sometimes necessary to see the motion, or make sure its vibrational amplitude is low enough for the signal to still be linear.

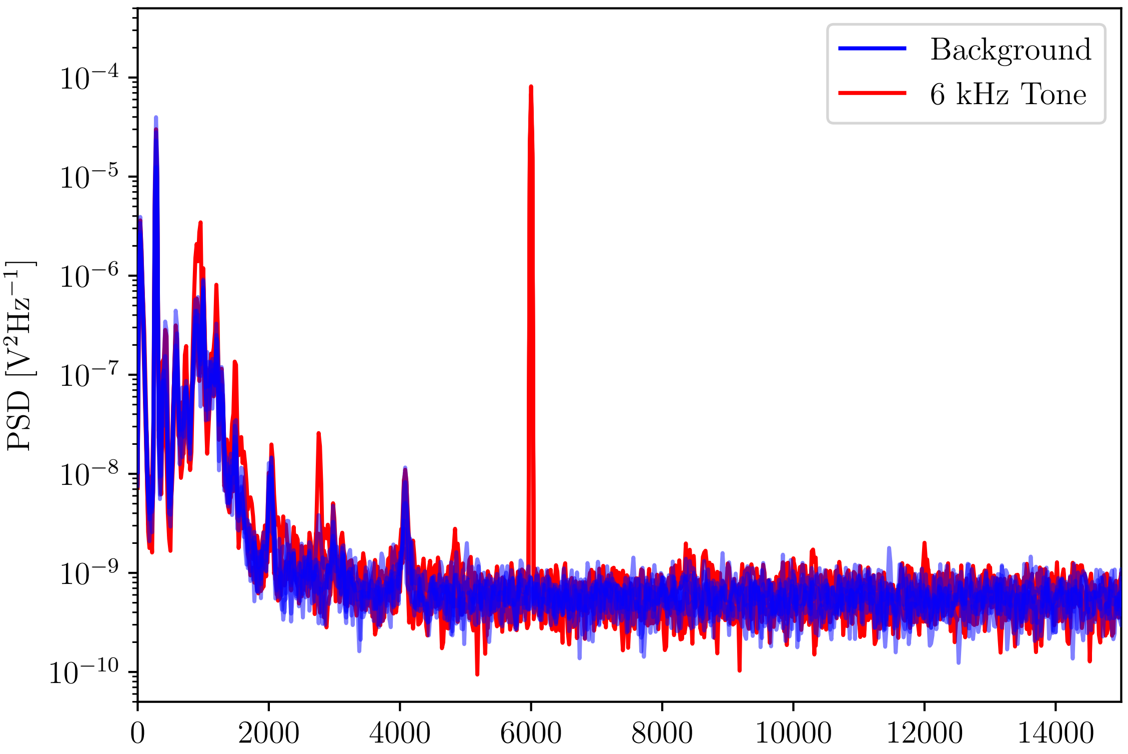

Figure 4.14: Power spectral density of the background (blue) with a tone of 6 kHz (red) shown in relation to it. Low frequency noise likely associated with vibrational and electrical noise with higher frequency noise flattening out.

Figure 4.15 shows the electrical impedance of the transducer with the different samples loaded onto it. This is done to obtain a base reference of motion for the samples with resonances of the transducer corresponding to the maximal motion of it. This data was obtained by measuring the current and voltage over the transducer as a fixed input voltage was sent to it, at frequencies of 100–15000 Hz. In general, the impedance follows a linear relation with frequency, with a slope coefficient $r = \Delta Z/\Delta f \approx 14.3\ \mu\Omega/\mathrm{Hz}$. As discussed in Section 3.2.2 this behaviour is expected of the coil-based transducer, whose impedance grows linearly with frequency, as seen in Figure 3.4. Here the impedances are instead shown in a logarithmic scale to better visualize the resonance peaks. The mirror and bulk samples (top) are shown in blue and yellow, respectively, with multiple resonance peaks observed below 6-7 kHz. This is something also shown for the c_1- and c_2-metamaterial samples (bottom), shown in green and red, respectively, with multiple resonances also shown below 7 kHz. At frequencies below these the comparisons between the different samples becomes more difficult, as resonance peaks are shifting around in both frequency and amplitude. For example, comparing the displacement of each respective sample at these frequencies becomes almost impossible, as any perceived attenuation is more likely caused by the increased motion at a resonance frequency of one sample that is not present for the other sample. However, since the metamaterial properties are mostly located at higher frequencies, this is not a major concern in that respect.

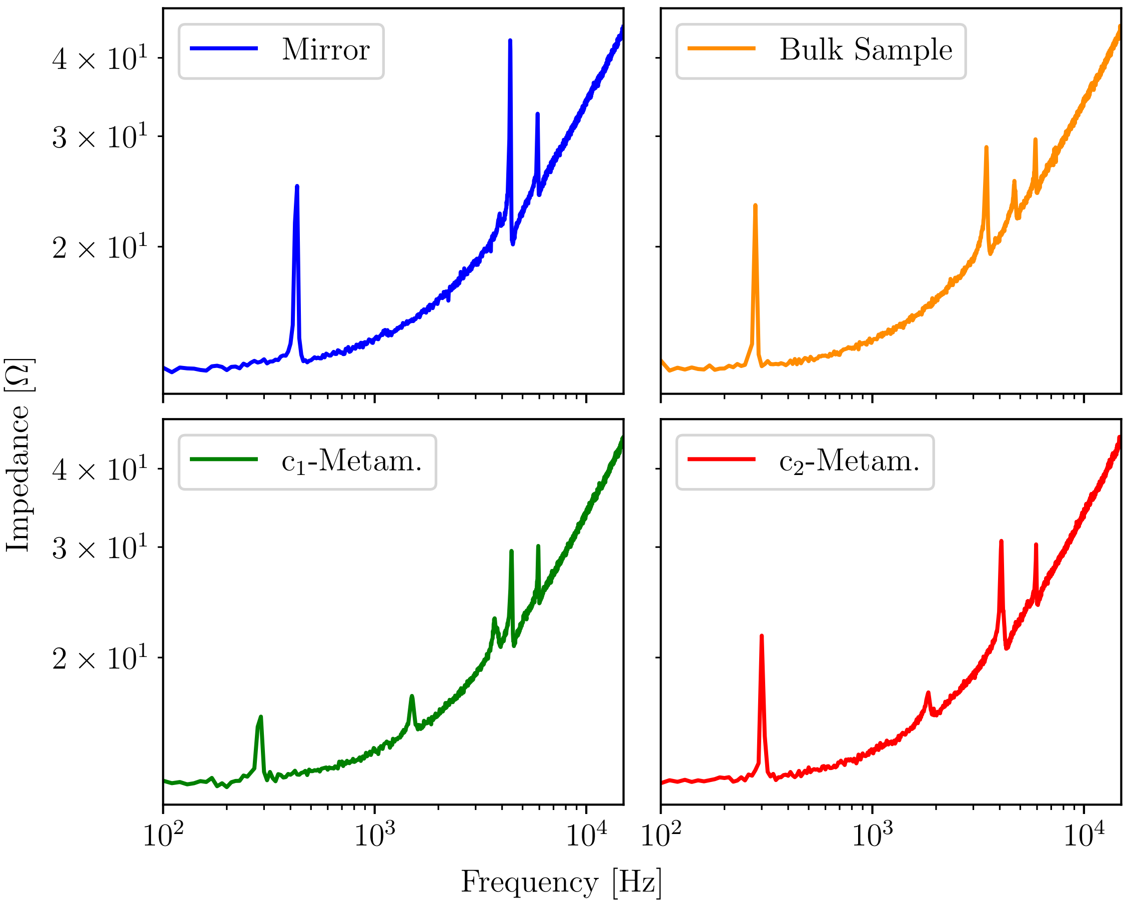

Figure 4.15: Transducer impedance as a function of frequency for each of the four studied samples, with the mirror (top left), bulk sample (top right), c_1- (bottom left) and c_2-metamaterials (bottom right). Multiple peaks can be observed corresponding to resonance frequencies of the transducer for each respective load.

Figure 4.16 shows the PID's frequency response, of its output signal, during closed-loop operation where the ratio between the homodyne signal amplitude and the output signal of the PID is plotted as a function of frequency. The input signal to the transducer was swept from frequencies of 10–2000 Hz with an input voltage of one volt. At low frequencies this ratio is low meaning that the PID is actively pulling the homodyne towards the phase quadrature locking meaning it is counteracting any motion of the transducer. However, at high frequencies this is not the case as the response flattens out, disregarding any resonance peaks caused by the transducer. This means that the voltage signal that is output by the photodetector is not representative of the motion of the transducer at lower frequencies, as it is significantly affected by the PID, but at higher frequencies this is not an issue.

4.3.1 Calibration of Homodyne

The calibration process of the homodyne, described in Section 3.2.4, was carried out by observing the output signal of the homodyne at two different input voltages of 100 millivolts and 20 volts (peak-to-peak) at frequencies of 500–1000 Hz. This frequency

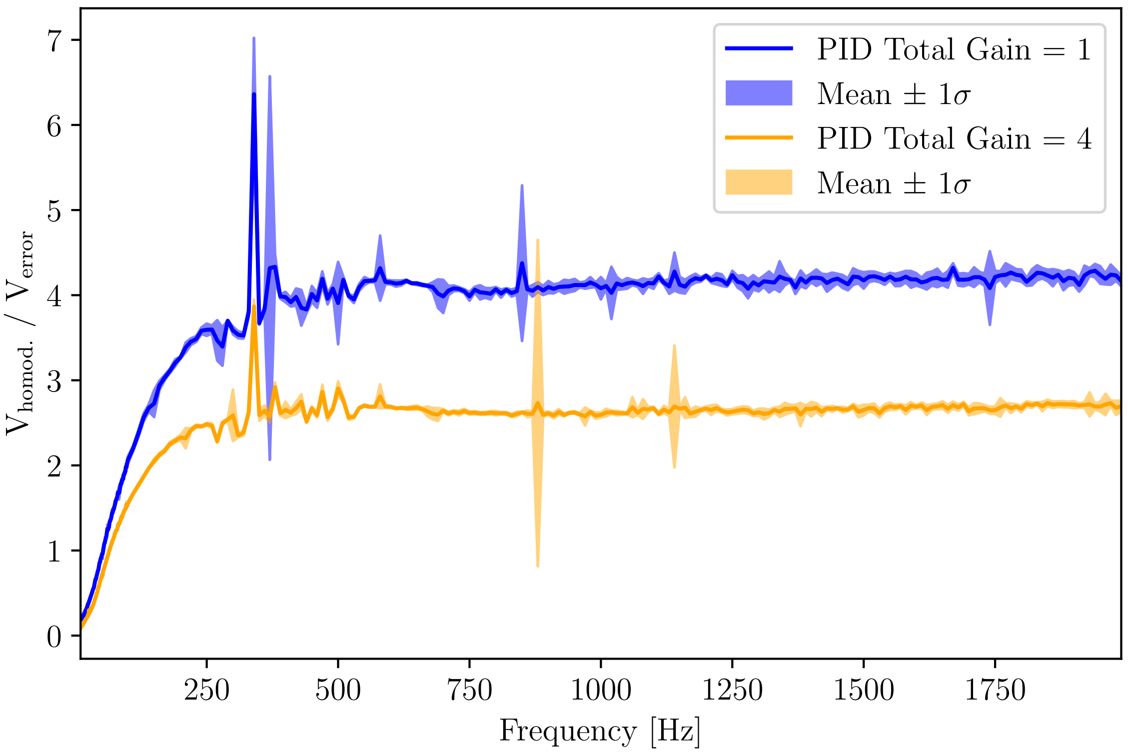

Figure 4.16: Closed-loop transfer function for the PID controller where the ratio between the homodyne and PID output voltages is shown against frequency, with a PID gain of one (blue) and four (orange). At low frequencies this ratio is low, meaning the PID can modulate the low frequency thermal drifts to lock to a stable phase quadrature. The response at higher frequencies, above 500 Hz, is flat, meaning the PID cannot keep up with the modulation. This results in motion of higher frequencies being unaffected by the PID.

sweep was chosen for three reasons: avoiding the effects of the PID controller, whose response is flat after 500 Hz, avoiding any resonances of the transducer, and because the calibration method could not be used at higher frequencies. The reason it could not be used has to do with moving the transducer a distance of $\lambda/2$. At higher frequencies, with this current setup, it was not possible to move the mirror by a distance large enough, see Section 3.2.2, to be able to count the fringes, meaning calibration fails at higher frequencies. Because of this, the assumption that the calibration is constant was made, with an average of the measurements at 500–1000 Hz being used to calculate the calibration constant for each sample. This resulted in the calibration shown in Figure 4.17, with the mirror and bulk sample shown in blue and orange, and c_1- and c_2-metamaterials shown in green and red, respectively. Shown is the mean of five measurements along with one standard deviation. The calibration values vary significantly between the samples, with, for example, the voltage to meter ratio for the c_1- and c_2-metamaterials varying by a factor of two, approximately. These discrepancies arise due to the alignment of the laser for the different samples, see Figure 3.3. If the laser alignment is not consistent between the samples, then the output signal will react differently to the same motion.

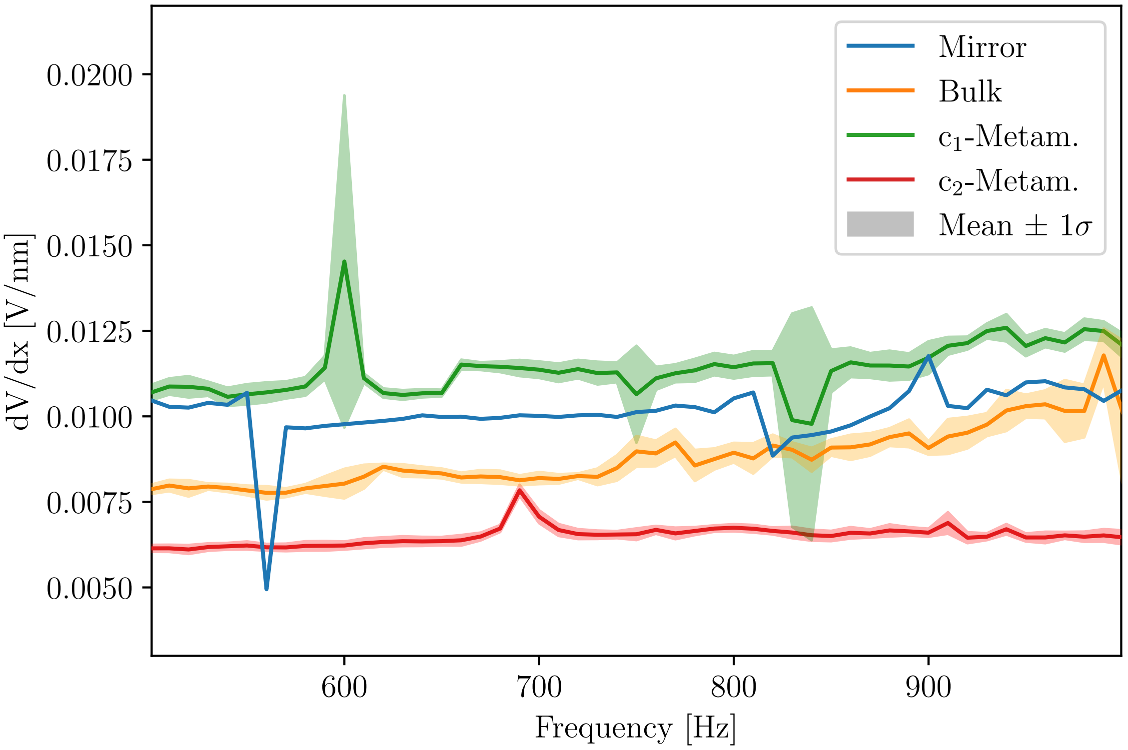

Figure 4.17: Results of the calibration of the optical interferometry, with the voltage to meter ratio shown as a function of frequency, in a frequency interval of 500–1000 Hz. The samples are shown in blue, orange, green, and red, corresponding to the mirror, bulk sample, and the c_1- and c_2-metamaterials, respectively. Each measurement was taken five times, with the mean and one standard deviation shown.

The alignment of the laser for the calibration, and other subsequent measurements, was made difficult due to the deformation of the fabricated samples, with no major issues noted with alignment when only the mirror was loaded where almost no drifts were noticed. First, during fabrication the samples had deformed, causing them to bend slightly. As the laser only sees the motion occurring perpendicular to its path, an angular offset in the mirror causes the motion observed to be incorrect. This could potentially be remedied with a thicker sample for future experiments, causing the sample to be less bendable. Secondly, the backreflected intensity was observed to drift in time, even as the transducer remained still, likely caused by mechanical vibrations of either mirrors, collimator, or the sample itself. This caused the fringe visibility of the output signal to vary in amplitude, as the information obtained from the motion drifted as well. Another consequence was the optimal PID set point changing with these drifts as well, with locking to the phase quadrature affected as a result. Most of these issues could likely be corrected for with a more robust alignment of the laser as well as minimizing any external mechanical vibrations.

4.3.2 Noise Floor Measurements

The noise floor of the system describes the minimum information that can be extracted through measurements. If the noise floor voltage is higher than the output signal voltage, that signal cannot be extracted. In this case it is a way to characterize the small motions the interferometer can detect from the transducer. Figure 4.18 shows the amplitude of the background noise at each frequency that has been translated to displacement via the calibration described in Section 4.3.1. This has resulted in a mostly flat response, with jumps in displacement amplitude at lower frequencies likely corresponding to frequencies of background vibrations, see Figure 4.14. At higher frequencies a small rise in displacement as frequency grows can be observed, with the noise floor for each respective sample following the same trend. In general, a measurement floor of about 100 to 200 picometres can be observed at frequencies above 5000 Hz, depending on the sample.

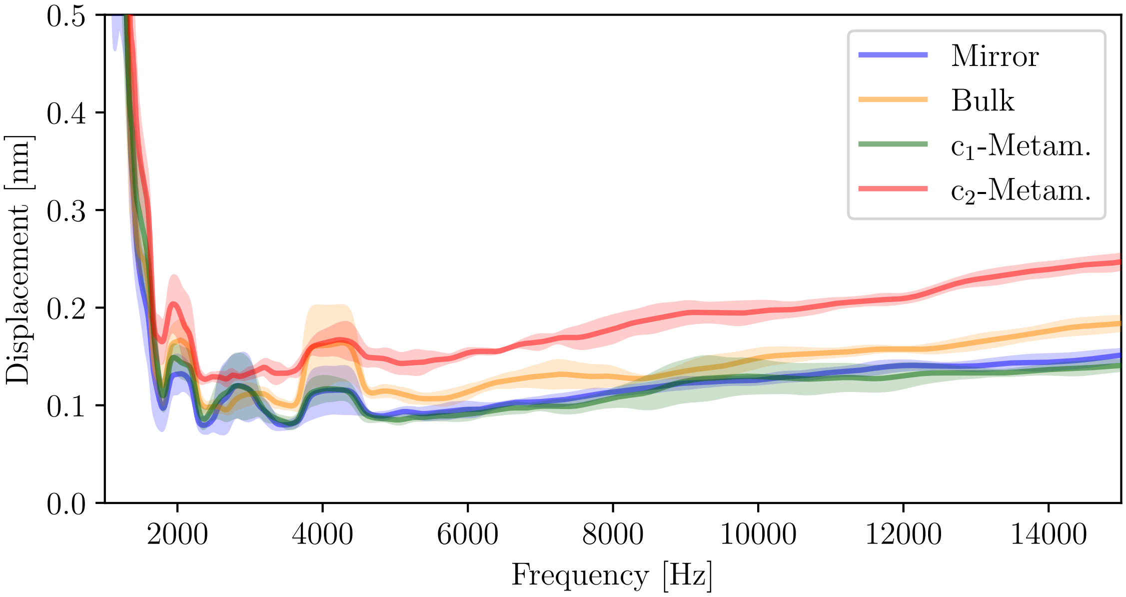

Figure 4.18: Noise floor measurements at frequencies of 1.0–15.0 kHz. Jumps in the noise floor at low frequencies correspond to peaks in background noise, while the response at higher frequencies is mostly flat.

4.3.3 Vibrational Displacement

Following the calibration measurements of the homodyne setup, the displacement measurements could be performed. These measurements were taken at drive voltages of 0.5 and 1.0 volts, at frequencies of 1.0–15.0 kHz. Five different measurement runs were performed with both the mean output voltage and its deviation from the mean being calculated. The voltage output signal of the homodyne could then be extracted from the oscilloscope with digital lock-in detection [47]. The displacement could then be calculated by dividing the amplitude of this signal with the mean calibration value obtained earlier for each respective sample. This voltage amplitude corresponds to the amplitude of the sinusoidal motion of the transducer.

Figure 4.19 shows the displacement of the mirror (top) and bulk sample (bottom) at the two input voltage levels, with a darker colour corresponding to a higher voltage, a shaded region corresponding to an error of one standard deviation, and the displacement noise floor (black). An inset of the displacement at higher frequencies is also shown (top right) for each sample, with a log-scale used to observe smaller details. The displacement of the mirror follows a path that is made up of many smaller dips with a general down-trending signal as frequency grows. As the error around the oscillating signal is smaller than the dips themselves they are correlated to the motion of the mirror and not caused by random noise in the system. The signal is completely above the noise floor for almost all frequencies, with a few exceptions where the signal falls into it. This is not the case for the bulk sample, as the signal does not exceed the noise floor above frequencies of roughly 12 kHz.

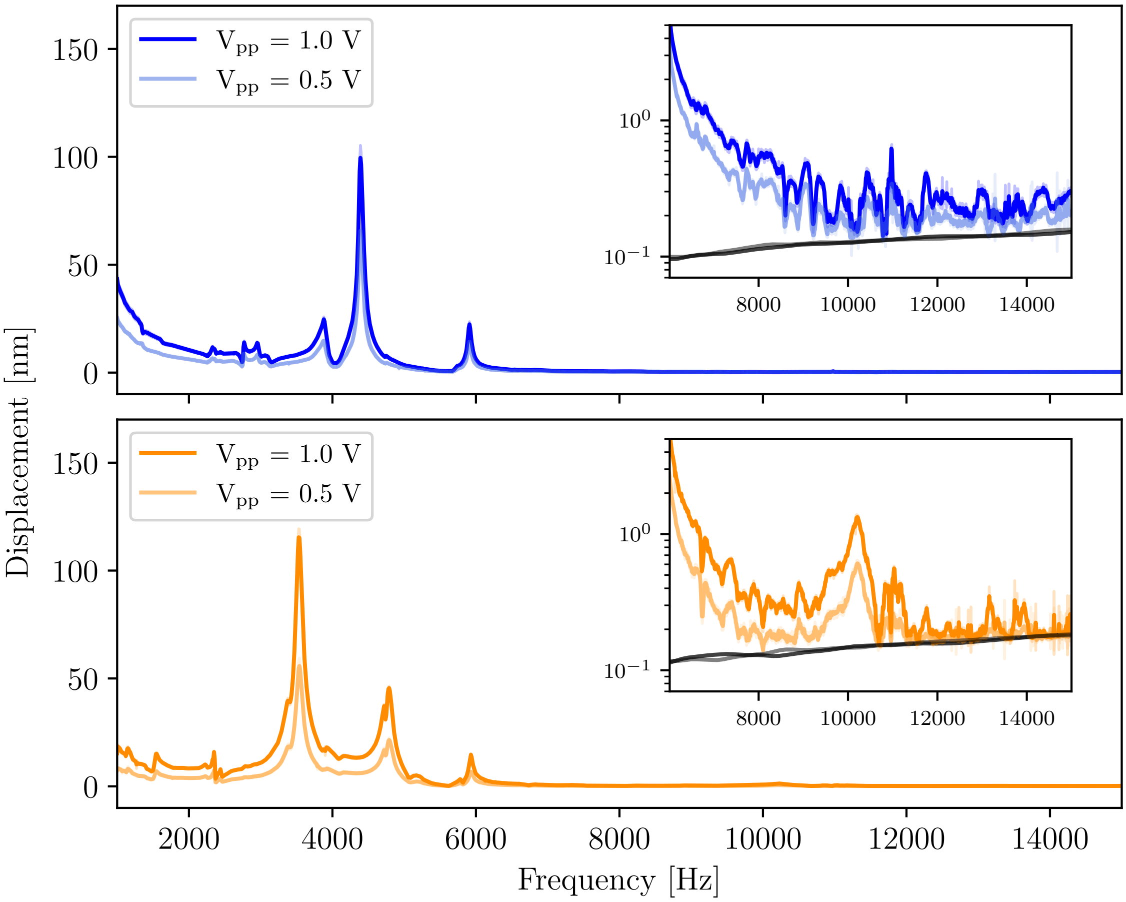

Figure 4.19: Displacements of mirror and bulk sample at frequencies of 1.0–15.0 kHz at input voltages of 0.5 and 1.0 volts. The insets (top right) for each sample shows the log-scaled displacement at higher frequencies.

Figure 4.20 shows the displacement of the c_1- (top) and c_2-metamaterial (bottom) samples at the two input voltage levels of 0.5 and 1.0 volts, with a darker colour corresponding to a higher voltage, and a shaded region corresponding to an error of one standard deviation. Here a much clearer correlation between the signal noise floor and the displacement is observed. As the metamaterials move the displacement measured is almost identical to the value of the noise floor. This is particularly clear in the case of a low input voltage, where the displacement more or less follows the floor at every frequency. This indicates that the true displacement of these samples are below the noise floor, meaning a maximum displacement of about 100 to 200 picometres in this range. This has the consequence of making the comparison between the bulk and metamaterial samples difficult, leading to only an upper bound of the displacement being able to be calculated at an input voltage of one volt. The displacement levels of the c_2-metamaterial sample is observed to be significantly higher than the c_1-metamaterial, as well as the noise floor, which is likely caused by discrepancies in the alignment of the samples.

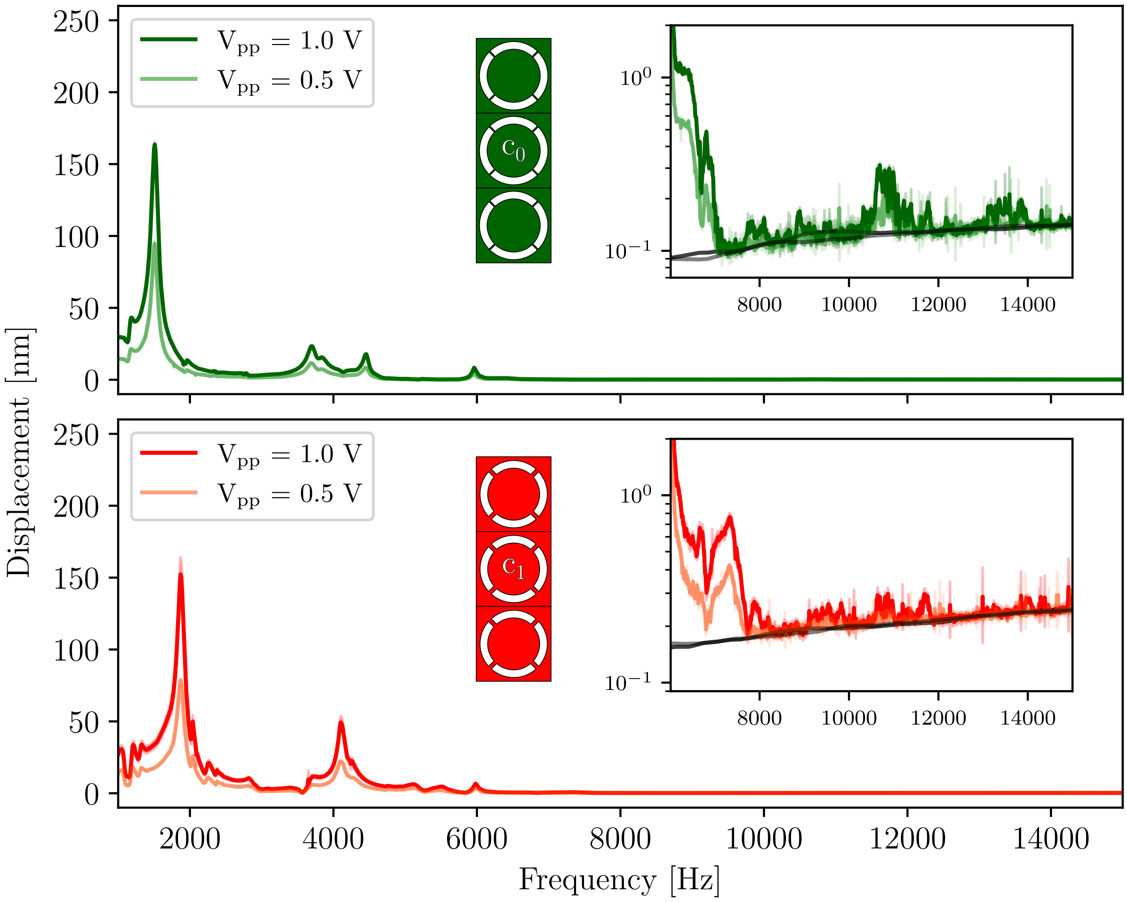

Figure 4.20: Displacements of metamaterial samples with c_1 (top) and c_2 (bottom) at frequencies of 1.0–15.0 kHz at input voltages of 0.5 and 1.0 volts. The insets (top right) for each sample shows the log-scaled displacement at higher frequencies.

4.3.4 Metamaterial Attenuation

To determine the attenuation caused by the metamaterial these displacements can be directly compared to one another. By simply dividing the observed displacement of one of the metamaterial samples by the displacement of the bulk sample the resulting ratio effectively describes the corresponding attenuation. True transmission, inverse of attenuation, can only be determined by measuring the displacement at the base and at the end of a single metamaterial sample, see Section 2.4. However, here an assumption is made that the bulk material serves as a reference instead, as it should not significantly affect the vibrations. The “transmission” can be defined as

$$\alpha = \frac{u_{\text{metam.}} - u_{\text{metam.}}^{\text{noise}}}{u_{\text{bulk}} - u_{\text{bulk}}^{\text{noise}}}, \tag{4.1}$$

where u_{sample}, $u_{\text{sample}}^{\text{noise}}$ are the displacement and displacement noise floor, respectively, of the measured sample. Subtracting the noise floor results in the true motion being measured, as it contains no information about the desired signal. If the signals are close to the noise floor, see Figure 4.19 and 4.20, this also means that α is not simply reflect a comparison of the noise floors of the respective samples. Figure 4.21 shows this relation between the bulk sample and mirror at frequencies of 1.0–15.0 kHz, for two different input voltages of 0.5 (lighter) and 1.0 (darker) volts. At frequencies of 6–9 kHz a mostly flat response can be observed, with larger peaks and dips around 4 kHz corresponding to resonances in the bulk sample and mirror, see Figure 4.19. The peak in transmission at roughly 10 kHz corresponds to a peak present in the displacement of the bulk sample but not in the displacement for the mirror.

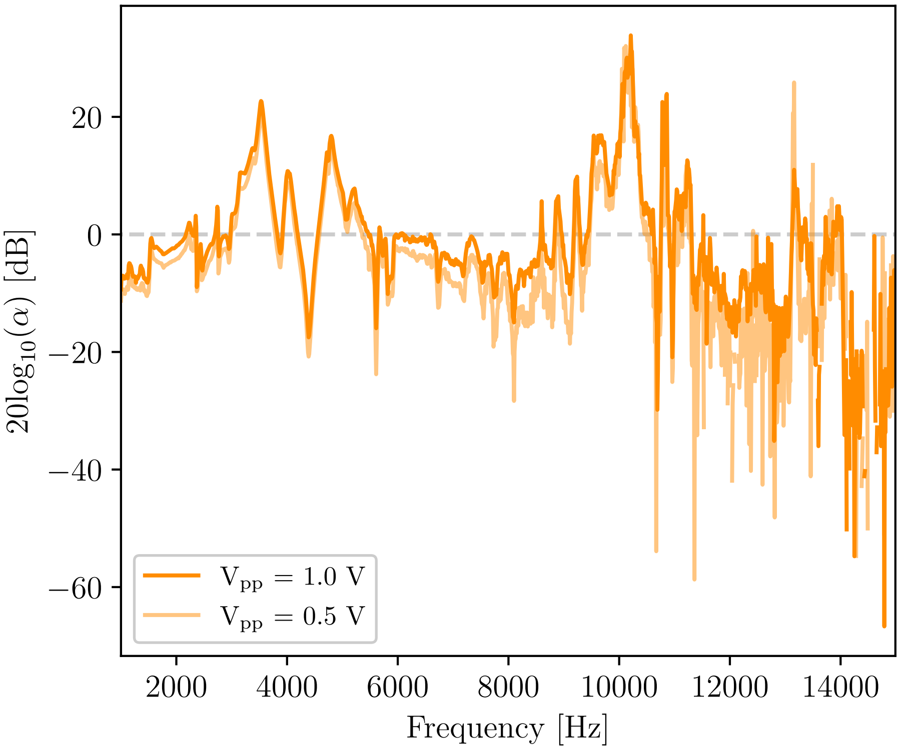

Figure 4.21: Transmission of the bulk sample compared with the mirror at two different input voltages of 0.5 and 1.0 volts.

Figure 4.22 shows the transmission of the two metamaterial samples, for c_1 (left) and c_2 (right), when compared to the bulk sample, at two different input voltages of 0.5 (lighter) and 1.0 (darker) volts. This is shown in a frequency interval of 6.0–15.0 kHz, with the transmission at lower frequencies dominated by different resonance peaks in the respective samples. There are some frequencies at which no data points can be seen, corresponding to the noise floor exceeding the measured signal, i.e., the transmission becoming negative. At a frequency interval of roughly 7.0–11.0 kHz a clear dip in the transmission of around -20 dB can be observed for the c_1-metamaterial, occurring from 8 kHz for the c_2-metamaterial with a slightly higher transmission level, around -10 to -15 dB. However, at 10 kHz, specifically, the dip likely corresponds to the aforementioned peak in the displacement of the bulk sample, since there is no such peak present in either of the metamaterial samples at that frequency. This does not seem to be the case at other frequencies, where the displacement of the bulk sample does not spike significantly, possibly indicating the result of attenuation caused by the metamaterial. As discussed earlier this comparison between the different samples can only result in an estimation of an upper bound of attenuation, with the metamaterial samples not exceeding the noise floor of the system. Another issue can be found in the difference in transmission at the different input voltages. As the transmission is a relative measurement of the displacement between samples, the input voltage should ideally not affect this. However, as the noise floor of the system is not exceeded at certain frequencies, in particular when the input voltage is too low, leading to apparent differences in transmission where none exist in reality.

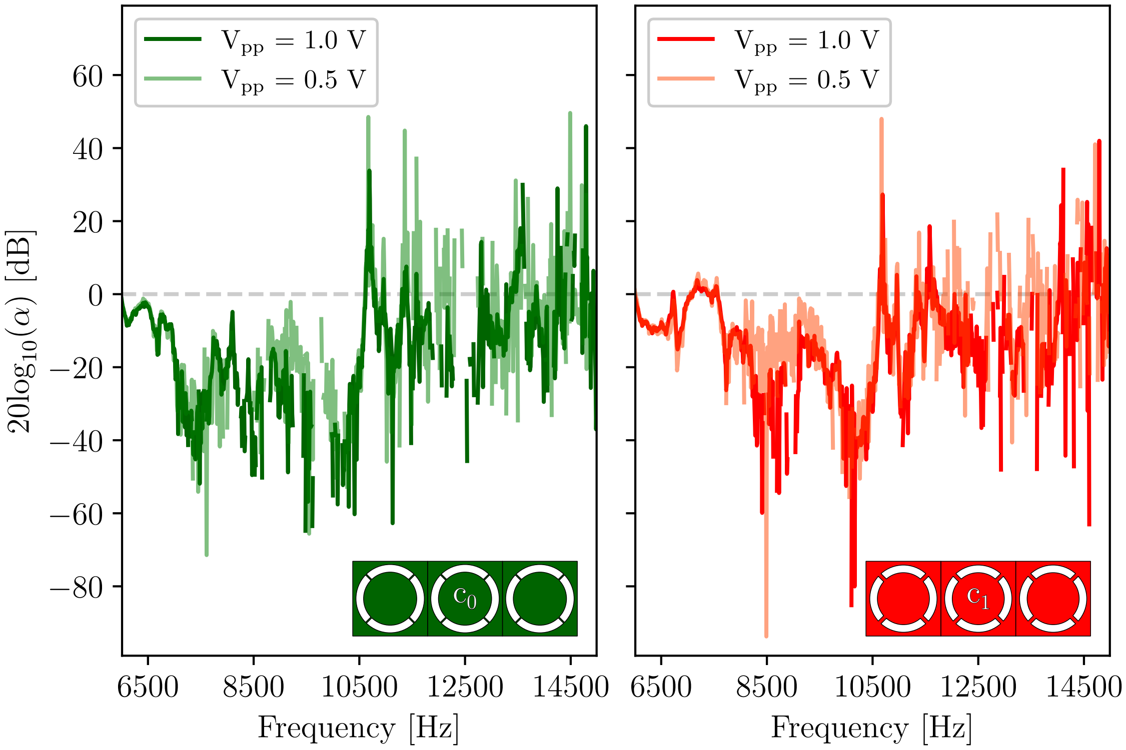

Figure 4.22: Transmission of c_1- (left) and c_2-metamaterial (right) samples compared with the bulk sample at two different input voltages of 0.5 and 1.0 volts.

5

Conclusion

In this thesis, the development of an acoustic metamaterial as a method of vibration isolation at cryogenic temperatures has been explored. Promising simulations of metamaterials with different materials and geometries have been performed, with initial simulations of metamaterial made from acrylic plastic showing band gap generation at around 10 kHz, with attenuation levels of 40 to 70 dB. Other simulated results show optimization of these band gaps, with composite structures, in particular, showing favourable results with band gaps found at frequencies below 4 kHz with the same geometry, with materials that could be more suitable for a low temperature environment. The variations and geometries of the studied samples have shown that optimization is possible with these materials, with significant changes in their phononic capabilities as a result of changing part of the structure to a different material, or changing the width of certain parts.

To achieve low frequency vibration attenuation a more complicated geometry would be a good starting point. For example, moving to a three dimensional geometry could be beneficial as it allows for more flexibility in design, and thus more opportunities for optimization as well. Already a two dimensional design has demonstrated a high flexibility in its phononic capabilities, with simple changes to it, either to its material composition or its geometry, resulting in significant changes occurring in the location of band gaps and the attenuation levels possible. By switching to three dimensions, this flexibility could result in the option to reduce the unit cell size as well, meaning greater attenuation could be achieved for a similar footprint.

An experimental setup has been designed to measure the vibrational displacement of a transducer. Successful measurements of the motion of a transducer have been performed, with mechanical resonances in its electric impedance showing as peaks in vibration amplitude. An upper bound of the attenuation could be calculated for the fabricated metamaterials, with attenuation levels of around 20 dB and 15 dB for the c_1- and c_2-metamaterials, respectively, in an interval of around 7.0–11.0 kHz. Further work will be required in order to fully realise the implementation of an acoustic metamaterial, with improvements in noise-suppression being of significant importance.

One immediate improvement to the experimental setup is to simply measure the transmission as is done in the simulations, with a mirror placed on the base of the metamaterial as well as the end of it, observing their motion individually and obtaining the corresponding attenuation. Another would be improving the alignment of the laser with the samples. If the alignment is not perpendicular to the sample then the motion observed by the laser becomes smaller, due to the angular offset, and therefore it becomes more difficult to exceed the noise floor of the system. By introducing more thorough alignment techniques, or aligning with greater care, could result in more consistent results across the homodyne setup. Other options to simply reduce the noise floor include thermal isolation, which could be achieved by placing the measurement in a vacuum-chamber, increasing the ratio between the LO and signal arm intensities, or improving the balance between the final beam splitter, see Figure 3.2, as it currently is not a perfect 50:50 split.

Future work can explore implementing such an acoustic metamaterial into a cryogenic environment to see how its acoustic isolation changes with lower temperatures as well as test its capabilities to replace or be integrated into already existing systems of vibration isolation. This would enable vibration isolation at specified frequency intervals, leading to more effective thermalization as well as a tuneable vibration attenuation that can be modified to work in different situations, i.e., when attenuation at a different frequency interval is desired, by swapping out one metamaterial for another.

Bibliography

[1] G. Ma and P. Sheng, Science Advances **2**, e1501595 (2016).

[2] N. Jiménez, O. Umnova, and J.-P. Groby, eds., *Acoustic waves in periodic structures, metamaterials, and porous media: from fundamentals to industrial applications*, Vol. 143, Topics in Applied Physics (Springer International Publishing, Cham, 2021).

[3] M. M. Sigalas and E. N. Economou, Journal of Sound and Vibration **158**, 377 (1992).

[4] M. Sigalas and E. N. Economou, Solid State Communications **86**, 141 (1993).

[5] M. S. Kushwaha, P. Halevi, L. Dobrzynski, and B. Djafari-Rouhani, Physical Review Letters **71**, 2022 (1993).

[6] Z. Liu, X. Zhang, Y. Mao, Y. Y. Zhu, Z. Yang, C. T. Chan, and P. Sheng, Science **289**, 1734 (2000).

[7] S. Zhang, L. Yin, and N. Fang, Physical Review Letters **102**, 194301 (2009).

[8] M. Lian, L. Duan, J. Chen, J. Jia, Y. Su, and T. Cao, Microsystems & Nanoengineering **8**, 108 (2022).

[9] M. Maldovan, Nature **503**, 209 (2013).

[10] M. Arndt and K. Hornberger, Nature Physics **10**, 271 (2014).

[11] O. Romero-Isart, L. Clemente, C. Navau, A. Sanchez, and J. I. Cirac, Physical Review Letters **109**, 147205 (2012).

[12] J. Prat-Camps, C. Teo, C. C. Rusconi, W. Wieczorek, and O. Romero-Isart, Physical Review Applied **8**, 034002 (2017).

[13] C. Timberlake, G. Gasbarri, A. Vinante, A. Setter, and H. Ulbricht, Applied Physics Letters **115**, 224101 (2019).

[14] M. G. Latorre, "Chip-based magnetic levitation of superconducting microparticles", PhD thesis (Chalmers University of Technology, 2022).

[15] H. Zu, W. Dai, and A. T. A. M. de Waele, Cryogenics **121**, 103390 (2022).

[16] J. P. Sethna, *Statistical mechanics: entropy, order parameters, and complexity* (Oxford University Press, Jan. 26, 2021).

[17] C. Nordling, *Physics handbook: for science and engineering*, Ninth edition (Studentlitteratur, Lund, 2020), 520 pp.

[18] W. Nolting and W. D. Brewer, *Fundamentals of many-body physics* (Springer Berlin Heidelberg, Berlin, Heidelberg, 2009).

[19] O. T. Bruhns, *Advanced mechanics of solids* (Springer, Berlin, Heidelberg, 2003).

[20] W. S. Slaughter, *The linearized theory of elasticity* (Birkhäuser Boston, Boston, MA, 2002).

[21] H. Ibach and H. Lüth, *Solid-state physics* (Springer, Berlin, Heidelberg, 1996).

[22] M. Periyasamy and N. Srinivasan, Results in Engineering **28**, 107660 (2025).

[23] G. N. Greaves, A. L. Greer, R. S. Lakes, and T. Rouxel, Nature Materials **10**, 823 (2011).

[24] G. Niraula, C. Wu, X. Yu, S. Malik, D. S. Verma, R. Yang, B. Zhao, S. Ding, W. Zhang, and S. K. Sharma, Journal of Materials Chemistry B **12**, 286 (2024).

[25] C. Uher, Journal of Superconductivity **3**, 337 (1990).

[26] J. Ekin, *Experimental techniques for low-temperature measurements: cryostat design, material properties and superconductor critical-current testing* (Oxford University Press, Oct. 12, 2006).

[27] H. M. Ledbetter, in *Advances in cryogenic engineering*, edited by K. D. Timmerhaus, R. P. Reed, and A. F. Clark (Springer US, Boston, MA, 1978), pp. 103–119.

[28] T. Middelmann, A. Walkov, G. Bartl, and R. Schödel, Physical Review B **92**, 174113 (2015).

[29] V. Laude, APL Materials **9**, 080701 (2021).

[30] S. Hu, L. Feng, C. Shao, I. A. Strelnikov, Y. A. Kosevich, and J. Shiomi, Physical Review B **102**, 024301 (2020).

[31] H. M. Ledbetter, Journal of Physics D: Applied Physics **13**, 1879 (1980).

[32] S. H. Lee and O. B. Wright, Physical Review B **93**, 024302 (2016).

[33] B. Xia, N. Chen, L. Xie, Y. Qin, and D. Yu, Applied Acoustics **112**, 1 (2016).

[34] J. Li and C. T. Chan, Physical Review E **70**, 055602 (2004).

[35] E. Cubukcu, K. Aydin, E. Ozbay, S. Foteinopoulou, and C. M. Soukoulis, Nature **423**, 604 (2003).

[36] S. Gröblacher, *Quantum opto-mechanics with micromirrors: combining nanomechanics with quantum optics*, Springer Theses (Springer, Berlin, Heidelberg, 2012).

[37] D. M. Pozar and D. M. Pozar, *Microwave engineering* (Wiley, Chichester, UNITED STATES, 2012).

[38] *How laser cutting is used in different industries*, `https://www.xometry.com/resources/sheet/how-is-laser-cutting-used-in-industry/`.

[39] P. Ciarlet and E. Lunéville, *The finite element method: from theory to practice*, 1st ed. (Wiley, Aug. 14, 2023).

[40] *COMSOL multiphysics®*, version 6.3.

[41] C. Shannon, Proceedings of the IRE **37**, 10 (1949).

[42] F. Resare, S. Islam Soke, and W. Wieczorek, Journal of Applied Physics **138**, 225304 (2025).

[43] M. A. Johnson and M. H. Moradi, eds., *PID control* (Springer-Verlag, London, 2005).

[44] W. Jiang, M. Yin, Q. Liao, L. Xie, and G. Yin, International Journal of Mechanical Sciences **190**, 106023 (2021).

[45] P. J. Rae and D. M. Dattelbaum, Polymer **45**, 7615 (2004).

[46] J. L. Jordan, C. R. Siviour, J. R. Foley, and E. N. Brown, Polymer **48**, 4184 (2007).

[47] *Principles of lock-in detection*, Zurich Instruments, (Dec. 20, 2019) `https://www.zhinst.com/europe/en/resources/principles-of-lock-in-detection/`.

DEPARTMENT OF MICROTECHNOLOGY AND NANOSCIENCE
CHALMERS UNIVERSITY OF TECHNOLOGY
Gothenburg, Sweden
www.chalmers.se

CHALMERS
UNIVERSITY OF TECHNOLOGY